

The High Latitude sNowfall Detection and Estimation aLgorithm for ATMS (HANDEL-ATMS): a new algorithm for the snowfall retrieval at high latitudes

Andrea Camplani¹, Daniele Casella¹, Paolo Sanò¹, Giulia Panegrossi¹

¹National Research Council of Italy, Institute of Atmospheric Sciences and Climate (CNR-ISAC), Via del Fosso del Cavaliere 100, 00133 Rome, Italy

Correspondence to: Andrea Camplani (Andrea.Camplani@artov.isac.cnr.it)

Abstract. Snowfall detection and quantification are challenging tasks in the Earth system science field. Ground-based instruments have limited spatial coverage and are scarce or absent at high latitudes. Therefore, the development of satellite-based snowfall retrieval methods is necessary for the global monitoring of snowfall. Passive Microwave (PMW) sensors can be exploited for snowfall quantification purposes because their measurements in the high-frequency channels (> 80 GHz) respond to snowfall microphysics. However, the highly non-linear PMW multichannel response to snowfall, the weakness of snowfall signature and the contamination by the background surface emission/scattering signal make snowfall retrieval very difficult. This phenomenon is particularly evident at high latitudes, where light snowfall events in extremely cold and dry environmental conditions are predominant. Machine Learning (ML) techniques have been demonstrated to be very suitable to handle the complex PMW multichannel relationship to snowfall. Operational microwave sounders on near-polar orbit satellites such as the Advanced Technology Microwave Sounder (ATMS), and the European MetOp-SG Microwave Sounder in the future, offer a very good coverage at high latitudes. Moreover, their wide range of channel frequencies (from 23 GHz to 190 GHz), allows for the dynamic radiometric characterization of the surface at the time of the overpass along with the exploitation of the high-frequency channels for snowfall retrieval. The paper describes the High Latitude sNow Detection and Estimation aLgorithm for ATMS (HANDEL-ATMS), a new machine learning-based snowfall retrieval algorithm developed specifically for high latitude environmental conditions and based on the ATMS observations.

HANDEL-ATMS is based on the use of an observational dataset in the training phase, where each ATMS multichannel observation is associated with coincident (in time and space) CloudSat Cloud Profiling Radar (CPR) vertical snow profile and surface snowfall rate. The main novelty of the approach is the radiometric characterization of the background surface (including snow covered land and sea ice) at the time of the overpass to derive multi-channel surface emissivities and clear-sky contribution to be used in the snowfall retrieval process. The snowfall retrieval is based on four different artificial neural networks for snow water path (SWP) and surface snowfall rate (SSR) detection and retrieval. HANDEL-ATMS shows very good detection capabilities - POD = 0.83, FAR = 0.18, and HSS = 0.68 for the SSR detection module. Estimation error statistics show a good agreement with CPR snowfall products for $SSR > 10^{-2}$ mm h⁻¹ (RMSE 0.08 mm h⁻¹, bias=0,02 mm h⁻¹). The analysis of the results for an independent CPR dataset and of selected snowfall events evidence the unique capability of HANDEL-ATMS to detect and estimate SWP and SSR also in presence of extreme cold and dry environmental conditions typical of high latitudes.

1 Introduction

Snowfall retrieval is one important topic in the atmospheric science field. On a global scale, snowfall represents only 5 % of the total global precipitation but it is predominant above 60-70 ° N/S (see *Levizzani et al, 2011*). In recent years, several studies have highlighted the strong influence of global warming on snowfall distribution and regimes, especially at high latitudes (see *Liu et al, 2009, Liu et al, 2012, Bintanja & Selten, 2014, Vihma et al, 2015*). However, global snowfall quantification is a challenging topic in weather sciences. Ground-based instruments such as raingauges or snowgauges provide only punctual measurements which can not fully capture the spatial variability of precipitation phenomena; moreover, the variability of snowflake shape and density has a strong influence on their fall speed and trajectories and therefore gauge-based measurements of falling snow result to be less accurate than for rain (see *Skofronick-Jackson et al, 2015*). Weather radars can provide areal measurements of precipitation - the rate estimation is based on the conversion of the measured backscattered radiation to precipitating hydrometeors content - but such operation presents some technical limitations (see *Kidd*

49 & Huffman, 2011). Finally, most of the regions where snowfall is predominant - such as Greenland, Siberia,
50 Canada, and Antarctica - are uninhabited or otherwise sparsely populated areas where weather observation
51 networks are very scarce or totally absent. Therefore, the development of satellite-based methods for snowfall
52 retrieval is necessary for global monitoring of snowfall. Passive Microwave (PMW) sensors on board polar
53 orbiting satellites can be exploited for snowfall detection purposes because the microwave (MW) signal is directly
54 responsive to the spatial distribution and microphysics properties of precipitation-sized hydrometeors in the
55 clouds; at the same time, the use of PMW sensors guarantees a high spatial coverage and high temporal resolution
56 (see Kidd & Huffman, 2011).

57 PMW snowfall detection and quantification is typically based on the ability to interpret the snowfall scattering
58 signature in the high frequency channels (> 90 GHz), which respond more effectively to ice microphysics and are
59 less prone to surface effects than low frequency channels, and to distinguish it from the clear-sky (surface and
60 atmosphere) contribution (e.g., Panegrossi et al, 2017). However, several factors make the PMW snowfall signal
61 ambiguous and the relationship between multichannel measurements and surface snowfall intensity highly non-
62 linear, especially in extremely cold/dry environmental conditions (see Panegrossi et al, 2022). The snowfall
63 scattering signal is relatively weak and is highly dependent on the complex microphysical properties of snowflakes
64 (Kim et al, 2008, Kulie et al, 2010, Kongoli et al, 2015), it is often masked by supercooled liquid water emission
65 signal (Wang et al, 2013, Battaglia & Delanoë, 2013, Panegrossi et al, 2017, Rysman et al, 2018, Battaglia &
66 Panegrossi, 2020, Panegrossi et al, 2022), and can be contaminated by the extremely variable background surface
67 emissivity (Liu and Seo, 2013, Takkiri et al., 2019, Rahimi et al, 2017), especially in cold and dry conditions
68 typical of the high latitude regions (Camplani et al, 2021). In this context, the availability of the latest generation
69 microwave radiometers - such as the conically-scanning radiometer GPM Microwave Imager (GMI) and the cross-
70 track scanning radiometer Advanced Technology Microwave Sensor (ATMS) - whose channels cover a wide
71 range of frequencies - offers new possibilities for global snowfall monitoring. The multi-channel PMW
72 observations can be used for both a dynamic radiometric characterization of the background surface - using the
73 low-frequency channels (< 90 GHz) - and for the detection and the estimation of the snowfall using the high-
74 frequency channels (> 90 GHz) (see Panegrossi et al, 2022).

75 The PMW capability to characterize physically and radiometrically the background surface varies from sea to
76 land, especially for the identification of cold/frozen surfaces. For what concerns the ocean, sea ice detection using
77 PMW observations has been a well-documented topic in the remote sensing science field since the 70s. This is
78 due to the strong contrast between sea ice (≈ 0.9) and open water (≈ 0.5) emissivity values at the MW low-
79 frequency range (~ 19 GHz) (see Comiso, 1983). Other studies highlighted the ability to discriminate between
80 different types of ice using a set of low-frequency window channels, because the differences between the
81 emissivities of the different types of sea ice increase with increasing frequency; in particular, at higher frequencies
82 (30-50 GHz) the contrast between the emissivity of “new” ice and “old” ice increases, with a decrease of the
83 emissivity at higher frequencies for “older” sea ice (see Comiso, 1983, Ulaby & Long, 2014). Moreover, it has
84 been observed that the simultaneous presence of open water and sea ice causes a decrease in the low-frequency
85 channel emissivity; the observed emissivity can be considered as a linear combination of the emissivity spectra of
86 sea ice and open water (see Ulaby & Long, 2014). For what concerns continental areas, the detection of snow-
87 covered land surfaces using MW measurements results to be more difficult. In dry conditions, a snowpack acts as
88 a volume scatterer; the scattering effect is dependent on the grain size and shape and on the depth of the snowpack
89 (see Clifford, 2010). However, the presence of liquid water can mask the scattering signature (see Mätzler &
90 Hüppi, 1989). At the same time, large areas of Greenland and Antarctica, while covered by dry snowpacks
91 throughout the year, do not show a significant difference between the two ATMS low frequency channels. Finally,
92 some snow-free areas, such as rocky mountains and cold deserts, present a scattering signature very similar to that
93 of the snowpack (see Grody & Basist, 1996). Therefore, the detection of snow-covered areas is very complex. A
94 set of several tests, each of which identifies snowpacks characterized by different physical and radiometric
95 characteristics, may be used.

96 This paper describes the development of a machine learning-based algorithm for snowfall retrieval (the High
97 Latitude sNowfall Detection and Estimation aLgorithm for ATMS, HANDEL-ATMS), exploiting ATMS
98 radiometer multi-channel measurements and using the CloudSat Cloud Profiling Radar (CPR) snowfall products
99 as reference. The algorithm has been developed focusing on the typical conditions of high latitude regions - low
100 humidity, low temperature, presence of snowpack on land or sea ice over ocean, and light snowfall intensity.

101 The main novelty of the approach is the exploitation of the ATMS wide range of channels (from 22 GHz to 183
102 GHz) to obtain the dynamic radiometric characterization of the background surface at the time of the overpass.
103 The derived surface emissivities are used to infer the clear-sky contribution to the measured TBs in the high
104 frequency channels in the snowfall retrieval process. This approach is similar to the work of *Zhao and Weng,*
105 *2002*, for AMSU observations limited to non-scattering surfaces (i.e., ocean and vegetated land), however the
106 application to surfaces with a very complex and time-varying emissivity (such as snow cover and sea ice) required
107 a far-away more advanced algorithm taking advantage of machine learning techniques. Moreover, the algorithm
108 is based on the exploitation of an observational dataset where each ATMS multichannel observation is associated
109 with coincident (in time and space) CloudSat CPR vertical snow profile and surface snowfall rate (hereafter
110 ATMS-CPR coincidence dataset).

111 Several snowfall retrieval algorithms for cross-track scanning radiometers have evolved in the last 20 years
112 starting from the Advanced Microwave Sounder Unit-B (AMSU-B) (*Zhao and Weng, 2002, Kongoli et al, 2003,*
113 *Skofronick-Jackson et al, 2004, Noh et al, 2009, Liu and Seo 2013*), and Microwave Humidity Sounder (MHS)
114 (see *Liu & Seo, 2013, Edel et al, 2020*), and evolving to ATMS (*Kongoli et al, 2015, Meng et al, 2017, Kongoli*
115 *et al, 2018, You et al, 2022, Sanò et al, 2022*). Some of them are based on radiative transfer simulations of observed
116 snowfall events (*Kongoli et al, 2003, Skofronick-Jackson et al, 2004, Kim et al, 2008*), or on in-situ data (see
117 *Kongoli et al, 2015, Meng et al, 2017, Kongoli et al, 2018*), others on CPR observations (*Edel et al, 2020, You et*
118 *al, 2022, Sanò et al, 2022*), or a combination of them (*Noh et al, 2009, Liu & Seo, 2013*). In the last five years,
119 there has been an increasing use of machine learning (ML) approaches trained on CPR-based coincidence datasets.
120 These approaches have proven to be very effective for snowfall retrieval. On one side, ML techniques are suitable
121 to handle the complex, non-linear PMW multichannel response to snowfall (e.g., *Rysman et al, 2018, Edel et al,*
122 *2020, Sanò et al, 2022*). On the other hand, the use of CPR-based datasets overcomes some of the limitations
123 deriving from the use of cloud-radiation model simulations, which are particularly challenging for snowfall events.
124 However, some limitations of the radar product used as a reference and issues related to the spatial and temporal
125 matching between the CPR and the PMW radiometer measurements introduce some uncertainty. Moreover, the
126 2CSP product is based on assumptions on snow microphysics, uses optimal estimation to retrieve snow
127 parameters, and uses a simplified radar reflectivity equation and is affected by CloudSat CPR limitations as
128 outlined in *Battaglia & Panegrossi, 2020*.

129 For what concerns ATMS, the ML-based Snow retrieval ALgorithm fOr gpM-Cross Track (SLALOM-CT)
130 (*Sanò et al, 2022*) has been developed within the EUMETSAT Satellite APplication Facility for Hydrology (H
131 SAF) in preparation for the launch of the EPS-SG Microwave Sounder (MWS). Similarly to HANDEL-ATMS, it
132 is trained on a ATMS-CPR coincidence dataset. SLALOM-CT is the evolution for cross-track scanning
133 radiometers of the Snow retrieval ALgorithm fOr GMI (SLALOM) (*Rysman et al, 2018, Rysman et al, 2019*)
134 which was the first ML algorithm for snowfall detection and retrieval for GMI trained and tested on GMI-CPR
135 coincident observations made available in the NASA GPM-CloudSat coincidence dataset (*Turk et al, 2021a*). One
136 of the novelties in the SLALOM (SLALOM-CT) approach is the use of the GMI (ATMS) low-frequency channels
137 to better constrain the snowfall retrieval to the characteristics of the surface at the time of the overpass (*Turk et*
138 *al, 2021b*). SLALOM-CT is based on a modular scheme, i.e., four separate modules are used for snowfall
139 detection, supercooled water layer detection, snow water path (SWP) and surface snowfall rate (SSR) estimate.
140 The predictor set is composed of the ATMS TBs and some environmental variables (T_{2m} , TPW, and principal
141 components derived from temperature and humidity profiles).

142 However, none of the algorithms mentioned here were tailored specifically to the extreme conditions typical of
143 high latitudes. The present work has the aim to develop an algorithm for snowfall detection and estimation by
144 exploiting the large frequency range typical of the last generation radiometers and to obtain a dynamic radiometric
145 characterization of the background surface at the time of the satellite overpass in order to highlight the complex
146 relationship between upwelling radiation and snowfall signature, which makes the detection very difficult in the
147 typical conditions of the high latitudes.

148 This article is organized as follows: Section 2 provides background information on ATMS and CPR, on the
149 methodology used to build the coincidence dataset and on the machine learning approaches used to develop the
150 algorithm. In Section 3 the algorithm structure is described. In Section 4 the overall performance scores are
151 reported and analyzed; a case study is analyzed and a comparison with SLALOM-CT is reported. Section 5 is
152 dedicated to the summary of the main results and to the conclusions.

153 **2. Instruments and methods**

154 **2.1 Advanced Technology Microwave Sounder (ATMS)**

155 ATMS is a total power cross-track scanning radiometer within 52.7° off the nadir direction. It has a total of 22
156 channels with the first 16 channels primarily used for temperature sounding from the surface to about 1 hPa (45
157 km) and the remaining channels used for water vapor sounding in the troposphere from the surface to about 200
158 hPa (10 km), and for cloud properties and precipitation retrieval. There are two receiving antennas: one serving
159 channels 1–15 below 60 GHz, and the other for channels above 60 GHz. The beamwidth changes with frequency
160 and is 5.2° for channels 1–2 (23.8–31.4 GHz), 2.2° for channels 3–16 (50.3–57.29 and 88.2 GHz), and 1.1° for
161 channels 17–22 (165.5–183.3 GHz). The corresponding nadir resolutions are 74.78, 31.64, and 15.82 km,
162 respectively. The outmost field of view (FOV) sizes are $323.1 \text{ km} \times 141.8 \text{ km}$ (cross-track \times along-track), 136.7
163 $\text{km} \times 60.0 \text{ km}$, and $68.4 \text{ km} \times 30.0 \text{ km}$, respectively (see *Weng et al, 2012*). ATMS is currently carried by three
164 near-polar orbiting satellites, Suomi National Polar-orbiting Partnership (SNPP) NOAA-20, and NOAA-21
165 providing global coverage including polar regions. Each satellite revisiting time is equal to 12 hours at the equator,
166 but drops to 100 minutes over the polar regions, ensuring a very high temporal resolution for the research area of
167 interest in this work. Moreover, the operational nature of the mission guarantees observations for the next decades.
168 It is worth noticing that the polarization of ATMS channels is not defined as vertical or horizontal, but as “Quasi-
169 Vertical” or “Quasi-Horizontal”. The “Quasi” prefix is used to indicate that ATMS (and any other cross-track
170 scanner) measures vertical or horizontal polarization only when looking at nadir and a mixture of V and H
171 polarization for off-nadir scan angles.

172 **2.2 Cloud Profiling Radar (CPR)**

173 The CPR is a 94 GHz nadir-looking radar onboard CloudSat. CloudSat was launched on April 28, 2006; the W-
174 band (94 GHz) Cloud Profiling Radar (CPR) operations began on June 2, 2006. CPR has been acquiring the first-
175 ever continuous global time series of vertical cloud structures and vertical profiles of cloud liquid and ice water
176 content with a 485-m vertical resolution and a 1.4-km antenna 3-dB footprint. The reference CloudSat snowfall
177 product is the 2C-Snow-Profile (2CSP) product (Version 5 is used in this work). It provides estimates of snowfall
178 characteristics for each observed profile. In particular, it provides an estimate of the Snow Water Path (SWP), i.
179 e., the total snow water content integrated over the atmospheric column, and of the Surface Snowfall Rate (SSR)
180 (see *Stephens et al, 2008*). SWP is estimated also when there is no snowfall at the ground level, therefore, the
181 presence of SWP is not always linked to the SSR, especially in warmer near-surface conditions (see *Wood &*
182 *L’Ecuyer, 2018*). 2CSP has several limitations, such as the contamination of the signal in the lowest 1000 - 1500
183 m of the profile due to ground-clutter, the underestimation of the heavy snowfall, due to attenuation of the radar
184 signal in these conditions, and the limited temporal sampling (although it is higher in the polar regions), and the
185 day-only operation mode since 2011, which limits its use during the winter seasons (see *Milani and Wood, 2021,*
186 *Panegrossi et al, 2022*). However, 2CSP has been demonstrated to be more accurate than GPM Dual-frequency
187 Precipitation Radar (DPR) snowfall products (see *Casella et al, 2017*) and in good agreement with estimates
188 obtained by ground-based radars (e.g., *Mroz et al, 2021*), although it is affected by underestimation for medium-
189 heavy snowfall events. Moreover, the polar orbit and the W-band high sensitivity make CPR suitable for snowfall
190 monitoring at higher latitudes (as demonstrated in several studies, *Kulie et al, 2016, Milani et al, 2018*) typically
191 characterized by light/moderate intensity (*Beranghi et al, 2016*).

192 **2.3 ATMS-CPR Coincidence Dataset**

193 The present study is based on a coincidence dataset between CPR and SNPP ATMS observations between January
194 2014 and August 2016. The same dataset has been used for the development of SLALOM-CT (*Sanò et al, 2022*).
195 Each coincidence comes from observations from CloudSat CPR and ATMS - onboard SNPP - within a maximum
196 15-minute time window. Moreover, the elements in the dataset have been selected by removing all corrupted data
197 and by applying an additional filter based on the minimum distance between CPR and ATMS IFOV center which
198 (22 km). The zonal distribution of the coincidences is due to the orbital geometry of CloudSat and SNPP, which
199 are both sun-synchronous with a relatively small difference in the satellite height (i.e., about 689 km and 833 km
200 for CloudSat and SNPP respectively). Therefore, the coincidence dataset is built from longer orbit fragments
201 (often semi-orbits) and by a very large number of elements near the poles. There is an asymmetry in the CPR
202 sampling between the Northern and the Southern hemisphere that can be observed in the dataset due to the CPR
203 daytime-only mode operation since 2011, which influences mostly the acquisitions in the Southern Polar region
204 (*Milani and Wood, 2021*).

205 The database has been built considering the horizontal resolution of the high-frequency channels of ATMS. The
206 CPR snowfall product used as reference is the 2CSP (V5). Some model-derived variables, specifically Total
207 Precipitable Water (TPW), the 2-m Temperature (T_{2m}), the Skin Temperature, the freezing level height and the
208 temperature and humidity profiles, have been added to the dataset to be used as ancillary parameters. Both 2D
209 and 3D environmental variables have been obtained from the European Center Medium Weather Forecast
210 (ECMWF). In particular, they are obtained from the CPR ECMWF-AUX product where the set of ancillary
211 ECMWF atmospheric state variable data is associated with each CloudSat CPR bin (the product is described by
212 *Partain, 2022*). Moreover, a cloud-cover fraction index, which indicates the fraction of CPR observations where
213 cloud is observed on the total CPR observations within each ATMS pixel, is added to the dataset.

214 Information about the presence of supercooled water is added in the coincidence dataset to be used towards the
215 correct interpretation of the snowfall signal in presence of supercooled water layers. The supercooled water
216 information has been extracted from the DARDAR product (see DARDAR). DARDAR, which stands for
217 raDAR+LiDAR, combines CPR radar and Cloud-Aerosol Lidar with Orthogonal Polarization (CALIOP) lidar
218 observations, onboard Cloud-Aerosol Lidar and Infrared Pathfinder Satellite Observations (CALIPSO) satellite,
219 and estimates both the cloud water phase and the ice water content and ice particle effective radius (see *Battaglia*
220 *& Delanoë, 2013, Ceccaldi et al, 2013*). In particular, the coincidence dataset includes an index indicating the
221 presence of supercooled cloud liquid water within each ATMS pixel, calculated as the fraction of DARDAR
222 observations where supercooled water within and on the top of the cloud is observed to the total DARDAR
223 observations within each pixel.

224 The association of ATMS TBs and CPR products has been done by averaging the CPR snow products with a
225 Gaussian function approximating the ATMS high-frequency antenna pattern (varying with the scan angle). It is
226 worth noting, however, that the ATMS IFOV is under-sampled by the narrow swath of the CPR (see *Sanò et al,*
227 *2022* for details). Moreover, it is worth noting that CPR 2CSP product limitations for snowfall detection and
228 estimation (see Section 2.2) might affect the ATMS-based snowfall estimates.

229 In this work, the dataset has been filtered based on humidity ($TPW < 10$ mm), temperature ($T_{2m} < 280$ K) and
230 elevation conditions (the working limits of the PESCA algorithm, see *Camplani et al, 2021*) leading to a good
231 representation of the higher latitudes with 80 % of the dataset elements located above $60^\circ N/S$. The dataset is made
232 of $2,14 \cdot 10^6$ elements, including $1,07 \cdot 10^6$ elements with falling snow ($2CSP\ SWP > 0$ kg m^{-2}) and $9,99 \cdot 10^5$ with
233 snowfall at the surface ($2CSP\ SSR > 0$ mm h^{-1}). The training and test phases have been conducted by splitting
234 randomly the dataset, with $\frac{1}{3}$ of the elements in the training and $\frac{2}{3}$ of the elements in the test dataset.

235 **2.4 Machine Learning approaches**

236 The algorithm is based on different machine-learning (ML) techniques. Moreover, clustering techniques have
237 been used to characterize from a radiometric point of view the background surface. In particular, an unsupervised
238 clustering technique has been used to identify emissivity clusters with small internal variability, and a supervised
239 clustering technique has been used to identify an emissivity spectrum based on other parameters.

240 **2.4.1 Artificial Neural Networks**

241 The HANDEL-ATMS snowfall detection and estimation modules have been developed using feedforward
242 multilayer neural network architectures, i. e., a neural network architecture where the neurons are arranged in
243 layers. This architecture, which is defined by the number of layers, the number of neurons for each layer, and the
244 transfer function of each neuron, has to be designed beforehand. The weights of connection links and the bias
245 values for each layer are estimated with a training process, based on the Levenberg–Marquardt algorithm (see
246 *Sanò et al, 2015*). The specific networks architecture, and the training and optimization procedure of the
247 HANDEL-ATMS algorithm are described in detail in section 3.2.

248 **2.4.2 Self Organizing Maps**

249 The unsupervised clustering method used for the background surface classification is the Self Organizing Map
250 (SOM) method (see *Faussett, 2006, Kohonen, 2012*). The characteristic of this method is that classes that are close
251 to each other from a topological point of view can be considered similar also from a physical and radiometric
252 point of view (see *Munchak et al, 2020*). SOMs have been used in previous studies for the classification of the
253 background surface by creating clusters based on emissivity values (see *Prigent et al, 2001, Cordisco et al, 2006,*
254 *Prigent et al, 2008, Munchak et al, 2020*).

255 2.4.3 Linear Discriminant Analysis

256 Several supervised clustering methods have been tested in this study, such as the linear discriminant analysis, the
257 quadratic discriminant analysis, the classification tree, and the nearest neighbor method. The final choice came
258 down to linear discriminant analysis (LDA, see *Hastie et al, 2009*) because this method guarantees satisfactory
259 accuracy in the results with a difference between the performances of the training and the test phase which is not
260 too significant, and a computational effort which is not too high.

261 3 Algorithm description

262 The configuration of the HANDEL-ATMS is summarized in the Flowchart in Figure 1. The process begins with
263 the classification of the background surface using the PMW Empirical cold Surface Classification Algorithm
264 (PESCA, *Camplani et al, 2021*); then, the surface emissivity spectra are derived through refinement process based
265 on LDA and these are used to estimate clear-sky simulated TB (TB_{sim}) using the ECMWF-AUX atmospheric
266 temperature and water vapor profiles. Then, the differences between the TB_{sim} and the ATMS observed TB (TB_{obs})
267 are evaluated ($\Delta TB_{obs-sim} = TB_{obs} - TB_{sim}$). Four ANNs are then applied to a predictor set consisting of ATMS TB_{obs} ,
268 $\Delta TB_{obs-sim}$, a surface classification flag, and other ancillary parameters (elevation and ATMS viewing angle for
269 the final version). Finally, the pixels classified with the presence of snowfall by the detection module, are used in
270 the estimation modules while for no-snowfall flagged pixels the snowfall rate value is set to 0 mm/h. In the
271 following sections the main blocks of the algorithm are described in detail.

272 3.1 Surface Classification and emissivity spectra estimation

273 3.1.1 PESCA Design and Performances

274 The dynamic classification and radiometric characterization of the background surface at the time of the satellite
275 overpass is based on PESCA exploiting ATMS low-frequency channels (*Camplani et al, 2021*). The algorithm
276 discriminates between frozen and unfrozen surfaces (sea ice and open water, snow-covered land and snow-free
277 land), and identifies 10 surface classes (4 over ocean, 5 over land, 1 for coast). The algorithm has been tuned
278 against the NOAA AutoSnow product (see *Romanov, 2019*), which gives daily maps of sea ice and snow cover.
279 For each ATMS observation, a flag reporting the AutoSnow class percentage (sea ice, open water, snow-covered
280 land, snow-free land) has been calculated; then, a threshold has been applied to discriminate between sea ice and
281 open water pixels (sea ice AutoSnow class > 10 %) and between snow-covered and snow-free land pixels (snow-
282 covered land AutoSnow class > 50 %). ATMS pixels have been classified into land, ocean, and coast pixels using
283 a land-sea mask.

284 The land module discriminates between snow-free land and snow-covered land and identifies four different snow
285 cover classes (Perennial, Winter Polar, Thin, and Deep Dry). It is based on a decision tree that makes use of a
286 limited number of inputs (the ratio TB_{23QV}/TB_{31QV} - **ratio**, the difference between TB_{23QV} and TB_{88QV} or Scattering
287 Index - **SI**, 23 GHz pseudo-emissivity (i. e. the ratio between an observed brightness temperature (TB) and a near-
288 surface temperature value) - **pem₂₃**). The module has been described by *Camplani et al, 2021*.

289 For what concerns the ocean module, a simple relationship to distinguish between sea ice and open water
290 observations has been identified. In Figure 2 a Cartesian plane where the x-axis represents 23 GHz observed TBs
291 and the y-axis represents the near-surface temperature (T_{2m}) is shown. In the figure each point represents a pseudo-
292 emissivity value, and the color describes the mean AutoSnow sea ice percentage within each bin (see Figure 2,
293 left panel). It is possible to observe that open water (0 % of sea ice, blue) and sea ice (100 % of sea ice, red) are
294 characterized by very different pseudo-emissivities. There is a transition area between open water and sea ice
295 pseudo-emissivity values for IFOVs where both open water and sea ice are present. The simple relationship for
296 sea ice identification is reported in the left panel as a green line where the condition for sea ice identification is
297 defined by Equation 1.

$$298 TB_{23QV} > T_{2m} - 96 K$$

299 (1)

300 Downstream of the sea ice/open water identification, information about sea ice characteristics is obtained from
301 the analysis of the two low-frequency pseudo-emissivity (**pem₂₃** and **pem₃₁**), which are a good approximation of
302 sea-ice emissivity for low-frequency channels especially in cold and dry conditions. In Figure 3 (top panel) it is
303 possible to observe that there are sea ice classified observations characterized by the contemporary presence of
304 open water and sea ice above the bisector of the plane and in correspondence with low emissivity values. In the
305 center panel, where the color represents sea ice occurrences, it is evident the presence of one cluster, in
306 correspondence with high pseudo-emissivity, with two “tails” above and below the bisector. This behavior has

307 been used to identify 3 different sea ice classes (New Sea Ice, Broken Sea Ice, and Multilayer Sea Ice) using a
 308 Nearest Neighbor Method based on a set of reference points that define the areas of interest for each sea ice class.
 309 In Figure 3 (bottom panel) a classification representation is reported, where the markers represent the reference
 310 points. The labels of the classes have been chosen by analyzing their physical properties and by comparing the
 311 estimated emissivity spectra with those reported in previous studies (*Hewison & English, 1999, Munchak et al,*
 312 *2020*).

313 PESCA's upper working limits for T_{2m} and TPW have been established to 280 K and 10 mm, respectively (see
 314 *Camplani et al, 2021* for details). Moreover, the land module does not work in the high elevation areas outside
 315 the polar regions (surface elevation > 2500 m for latitude < 67 ° N/S) because the ATMS low spatial resolution
 316 does not allow for depicting the small-scale snow-cover variability that characterizes the orographic regions. An
 317 analysis carried out using the ATMS-CPR coincidence dataset highlights that the presence of cloud cover does
 318 not influence the overall PESCA performances (not shown). Within these well-defined limits, the PESCA
 319 manages to optimally discriminate between sea ice, open water, snow-free land and snow-covered land. The
 320 statistical scores of PESCA identification of sea ice and snow cover (using AutoSnow as the reference) are
 321 summarized in Table 1. In particular, the Probability of Detection (POD), the False Alarm Ratio (FAR), and the
 322 Heidke Skill Score (HSS) are reported. POD, FAR, and HSS are defined by equations 2,3 and 4.

$$323 \quad POD = \frac{h}{h+m}$$

324 (2)

$$325 \quad FAR = \frac{f}{f+h}$$

326 (3)

$$327 \quad HSS = \frac{2(h*cn - f*m)}{(h+m)*(m+cn) + (h+f)*(f+cn)}$$

328 (4)

329 where h represents the hits, f represents the false alarms, m represents the misses and cn represents the correct
 330 negatives. PESCA manages to optimally detect the presence of a frozen background (sea ice over the ocean, snow
 331 covered land over the continental part) at the time of the satellite overpass. It is important to underline that the
 332 variability of the HSS compared to POD and FAR is due to the different number of correct negatives. An analysis
 333 of the physical characteristics of the PESCA classes has been conducted by considering the mean T_{2m} , the
 334 geographical and seasonal distribution associated with each class. For what concerns the land classes, please refer
 335 to *Camplani et al, 2021*. For what concerns sea ice, the New Sea Ice class, which is detected during the winter at
 336 high latitudes and for low temperatures, represents the sea ice that forms during the winter. The Broken Sea Ice
 337 class, which is predominant in the lower latitudes and whose occurrence increases during the Spring season,
 338 represents the co-presence of sea ice and water. The Multilayer Sea Ice class, which is detected only at the high
 339 latitudes, for very low temperatures, and constantly throughout the year, represents the ice pack typical of those
 340 regions and extreme cold conditions.

341 3.1.2 PESCA emissivity spectra estimation

342 The emissivity spectra of each class have been estimated by applying the PESCA algorithm to the cloud-free (0%
 343 CPR cloud mask fraction) ATMS observations in the ATMS-CPR dataset satisfying PESCA working limits. The
 344 ATMS clear-sky TBs measured for each PESCA surface class have been used as input to an inverse radiative
 345 transfer model (RTM) based on plane-parallel approximation (*Ulaby & Long, 2014*) and the *Rosenkrantz (1998)*
 346 gas absorption model. The emissivity spectra have been estimated by calculating the mean and the standard
 347 deviation of the emissivity values for each class (excluding the values lower than the 10th percentile and higher
 348 than the 90th percentile). The emissivity spectra dependence on the ATMS viewing angle for polarized surfaces
 349 has been neglected because an analysis of such dependence in the ATMS-CPR coincidence dataset has shown
 350 that it is not significant (emissivity difference smaller than 0.05 for angles up to 52.7 °). This is due to the fact
 351 that cross-track scanning radiometers measure a signal (off-nadir) which derives from a mixture between the two
 352 polarizations (e.g., quasi-vertical, QV, and quasi-horizontal, QH). As a consequence, although the emissivities of
 353 polarized surfaces, such as open water surfaces, are strongly influenced by the viewing angle, the emissivity
 354 variation is compensated by the effect of the mixture of the two polarizations (see also *Felde & Pickle, 1995,*
 355 *Prigent et al, 2000, Mathew et al, 2008, Prigent et al, 2017*).

356 The estimated spectra are shown in Figure 4 and Figure 5 for ocean and land classes respectively (the coast has
 357 also been considered as a separate class, however its spectrum is not shown in Figures 4-5). It is possible to

358 observe that the classes are well-characterized from a radiometric point of view, showing distinct behavior of the
 359 emissivity spectra (e.g., the mean values). However, all the classes present significant standard deviations at high
 360 frequency, and some classes - such as the snow classes and the Broken Sea Ice class - present a high value of
 361 standard deviation also at low frequency.

362 The clear-sky RTM simulations based on the mean emissivity values estimated for each class, have been compared
 363 to the coincident observed clear-sky TBs. - but the RMSE between simulated and observed clear-sky TBs appeared
 364 to be too high to implement a robust signal analysis (>10 K). For this reason, a refinement process for the
 365 emissivity spectra estimation based on machine learning techniques has been developed downstream of the
 366 PESCA classification.

367 The refinement process has been based on a combination of an unsupervised classification technique (SOM) and
 368 a supervised technique (LDA). The unsupervised classification identifies clusters characterized by the minimum
 369 inner variability from a radiometric point of view. The supervised technique, instead, has the goal to identify the
 370 previously obtained clusters, and the associated emissivity spectra, by using only input variables that are not
 371 affected by the presence of clouds. The final emissivity spectra are estimated as the mean emissivity for each
 372 frequency within each cluster identified by the supervised technique. Therefore, as first step, the emissivity
 373 spectra have been clusterized in order to minimize the emissivity variability in each cluster by arranging the
 374 retrieved emissivity values for six ATMS channels (23.8 GHz, 31.4 GHz, 50.3 GHz, 88.2 GHz, 165.5 GHz, and
 375 183.31 ± 7 GHz) in a one-dimensional SOM architecture. Then, an LDA model has been trained using the
 376 previously obtained clusters as reference and using the PESCA input parameters (**pem₂₃**, **pem₃₁**, **ratio** and **SI**),
 377 some environmental parameters (**TPW**, **T_{2m}**, surface pressure - **P_{surf}**) and ancillary variables (latitude - **lat**, Julian
 378 day - **jd**, altitude - **DEM**, the maximum solar height during the day - **H_{sun}**) as input. The use of the LDA is
 379 necessary to associate an emissivity spectrum to all the observations which are classified by PESCA,
 380 independently of the presence of clouds. It is worth noticing that the whole predictor set of the LDA has resulted
 381 to be redundant; therefore, a subset of the predictors has been selected for each class. The accuracy of the LDA
 382 classification is given by the ratio between the number of hits (observations where LDA identifies the associated
 383 SOM class) and the total number of observations; it can be considered as an indicator of the effectiveness of the
 384 LDA model in rebuilding the SOM results.

385 The evaluation of the refinement process is based on the comparison between the simulated clear-skyTBs and the
 386 observed clear-sky TBs for each PESCA surface class. For each PESCA surface class, the number of clusters that
 387 simultaneously lowers the errors (RMSE) between the simulated and observed clear-sky TBs at high frequency
 388 (without lowering the classification accuracy too much) is chosen.

389 In Table 2 the number of clusters, the predictors selected, the accuracy, RMSE and percentage normalized root
 390 mean squared error (NRMSE%) (*Gareth et al, 2013*) estimated on the test dataset, are reported for the 165.5 GHz
 391 channel. NRMSE% is defined by Equation 5.

$$392 \quad NRMSE_{\%} = \left(\frac{RMSE}{\sigma} * 100 \right)$$

393 (5)

394 where σ represents the standard deviation of the measured clear-sky TBs dataset in each PESCA class. It can be
 395 considered an indicator of the effectiveness of the refinement process.

396 For some classes, such as the Ocean class, the refinement process leads to low RMSE values (< 4 K). For other
 397 classes, such as Deep Dry Snow and Broken Sea Ice, RMSE remains > 5 K even with a high number of clusters,
 398 although there is a significant reduction compared to the initial variance in each class (NRMSE% < 50). This is
 399 due to the variability of snow-covered background within each class; in the worst scenario, the limited number of
 400 predictors are insufficient to infer the emissivity spectrum at high frequency. Overall, the refinement process
 401 allows to obtain a general improvement of the accuracy of the dynamic emissivity estimation for the PESCA
 402 classes; however, for some classes, the high-frequency channel uncertainty remains significant. The emissivity
 403 spectra obtained by PESCA refinement are used as inputs of the RTM to obtain clear sky simulated TBs (TB_{sim})
 404 to be compared to the actual observations (TB_{obs}). The comparison between TB_{sim} with TB_{obs} allows to highlight
 405 and interpret the MW signal in presence of snowfall.

406 In Figure 6, the snowfall signal is represented as a function of the SWP for the 165.5 GHz channel and for different
 407 PESCA classes. The red line and shaded areas represent the mean values and standard deviations of the difference
 408 between TB_{obs} and TB_{sim} ($\Delta TB_{obs-sim} = TB_{obs} - TB_{sim}$) for SWP bins calculated for observations where 2CSP SWP
 409 > 0 kg m⁻². The blue lines represent the uncertainty due to surface emissivity variability for each PESCA. They

410 are centered on the estimated bias for each class (close to 0 K) and the dashed lines correspond to the standard
 411 deviation of $\Delta TB_{\text{obs-sim}}$ in clear sky conditions. A clear scattering signal ($\Delta TB_{\text{obs-sim}} < 0$) is observed over all the
 412 classes considered for intense snowfall events ($\text{SWP} > 1 \text{ kg m}^{-2}$). For lower SWP values, the signal is more
 413 ambiguous and changes with the background surface. While over Land there is a clear scattering signal for SWP
 414 $> 0.1 \text{ kg m}^{-2}$, over the Perennial Snow class a scattering signal can be observed only for $\text{SWP} > 0.5 \text{ kg m}^{-2}$. For
 415 $\text{SWP} < 0.1 \text{ kg m}^{-2}$, the mean $\Delta TB_{\text{obs-sim}}$ for snowfall observations is less than its standard deviation in clear sky.
 416 This is due mainly to the emissivity variability for each surface class, and to the error introduced by the use of
 417 model-derived temperature and water vapor profiles in the RT simulations. However, while for the Land class the
 418 mean $\Delta TB_{\text{obs-sim}} < 0 \text{ K}$ can be explained as a predominant scattering effect for all SWP values, for the Perennial
 419 Snow class the mean $\Delta TB_{\text{obs-sim}} > 0 \text{ K}$ can be interpreted as a predominant emission signal with respect to the
 420 radiatively cold background (Figure 5). The Thin Snow class shows an intermediate behavior: for $\text{SWP} < 0.1 \text{ kg}$
 421 m^{-2} the red shaded area within the RMSE limits (blue lines) of the RT simulations denotes the difficulty in
 422 interpreting the signal, while a clear scattering signal can be observed for $\text{SWP} > 0.3 \text{ kg m}^{-2}$. For what concerns
 423 ocean and new sea ice classes, a clear scattering signal is visible only for high SWP values ($> 1 \text{ kg m}^{-2}$) while for
 424 low SWP values a significant emission signal is observed. It is very likely that the emission effect observed over
 425 ocean and sea ice is generated by supercooled cloud liquid water. The ubiquitous presence of supercooled water
 426 layers in snowing clouds (see Wang *et al*, 2013, Battaglia & Panegrossi, 2020), especially over oceans (see
 427 Battaglia & Delanoë, 2013), generates an emission effect which is particularly significant over radiatively cold
 428 surfaces (such as Perennial Snow, Ocean and New Sea Ice at high frequency, see Figure 4), and can mask or
 429 overcome the weak scattering signal generated by falling snow especially in light snowfall events. It is also
 430 important to underline that the DARDAR product identifies mostly supercooled water layers at the cloud top
 431 (Rysman *et al*, 2018, Panegrossi *et al*, 2017), while it has been shown that the impact of supercooled water layers
 432 embedded in the clouds can be very significant on the measured TBs at MW high frequency window channels
 433 (Battaglia & Panegrossi, 2020, Panegrossi *et al*, 2022).

434 3.2 ANN Design for snowfall retrieval

435 The snowfall detection and estimation modules have been based on ANNs. Four ANNs have been developed: two
 436 for the detection of SWP and SSR and two for the SWP and SSR estimate. The performance of more than 50
 437 architectures have been tested, by varying the number of layers, the number of neurons for each layer, and the
 438 activation functions. The final architecture, for all modules, is composed of four layers: an input layer with a
 439 neurons number equal to the predictor number, and a hyperbolic tangent function as the activation function, a first
 440 hidden layer (60 neurons), and hyperbolic tangent function, a second hidden layer (30 neurons), with a sigmoid
 441 function (for more information about the Neural Network characteristics, see Sanò *et al*, 2015). At the same time,
 442 several predictor sets have been tested combining in different ways ATMS TB_{obs} , $\Delta TB_{\text{obs-sim}}$, PESCA surface
 443 class, ATMS angle of view, ancillary information (surface elevation from a Digital Elevation Model), and model-
 444 derived environmental variables (T_{2m} , TPW, and freezing level height). In Table 3 the statistical scores of the
 445 algorithm performance for the SSR detection module obtained for different predictor sets are reported. It is
 446 possible to see that the best performance is obtained when the predictor set is composed of ATMS TB_{obs} and
 447 $\Delta TB_{\text{obs-sim}}$, (besides PESCA surface flag, the pixel elevation and the cosine of the viewing angle). In particular, it
 448 is notable the improvement of the detection capabilities with respect to a predictor set composed of ATMS TB_{obs}
 449 and environmental parameters. On the other hand, the simultaneous use of both the $\Delta TB_{\text{obs-sim}}$ and the
 450 environmental parameters show scores almost equal to that obtained by using only $\Delta TB_{\text{obs-sim}}$. This indicates that
 451 the computation of the multi-channel clear-sky TBs at the time of the overpass through the estimation of the
 452 dynamic surface class emissivity spectra and its deviation from the measured TBs plays a fundamental role in
 453 snowfall retrieval. It provides essential information to the ANN to be able to exploit the subtle snowfall-related
 454 signal in ATMS measurements. This is the most innovative aspect of HANDEL-ATMS.

455 Based on these results, the final set of predictors for HANDEL-ATMS is composed by 16 ATMS channels TB_{obs}
 456 (1-9, 16-22, channels 10-15 have not been considered because their weighting function peaks above the
 457 tropopause), and the corresponding $\Delta TB_{\text{obs-sim}}$, the PESCA classification flag, the pixel elevation (obtained from
 458 a DEM) and the cosine of the view angle.

459 4. Results

460 4.1 HANDEL-ATMS Performances

461 In Table 4 the statistical scores of HANDEL-ATMS detection module performances are reported in terms of POD,
462 FAR and HSS. It is possible to observe good detection capabilities both for SWP and SSR modules (POD > 0.8,
463 FAR < 0.2).

464 In Figure 7 and in Figure 8 the dependence of HANDEL-ATMS snowfall detection statistical scores on TPW and
465 on T_{2m} is reported. In both figures, it is possible to observe that the SWP detection capabilities improve (with an
466 increase of POD and HSS and a decrease of FAR) with increasing humidity and temperature. This is due to the
467 combined effect of a stronger scattering signal associated with more intense snowfall events - linked to moister
468 and warmer environmental conditions - and to the lower transmissivity of the atmosphere which masks the
469 background surface signal, reducing its impact and the uncertainties linked to its variability. On the other hand,
470 colder and drier conditions are usually linked to background surface types characterized by high radiometric
471 variability such as Perennial Snow and Winter Polar Snow classes, which cause uncertainty in emissivity
472 estimation. It is possible to observe that in Figure 7 SSR detection capabilities show a maximum HSS value for
473 TPW between 3 mm and 5 mm, and then there is a slight decrease due to the decrease of POD. A similar situation
474 can be observed in Figure 8, where the HSS reaches a maximum between 250 K and 275 K, and it is lower than
475 for SWP. This is due to the fact that PMW measurements respond mostly to the snow in the atmospheric column
476 and in moister/warmer conditions the presence of snow in the atmosphere is not always linked to surface snowfall.
477 In both cases, it is worth noting that also considering very dry (TPW \approx 2 mm) or very cold ($T_{2m} \approx$ 240 K)
478 conditions, HANDEL-ATMS shows good detection capabilities, in spite of the uncertainties linked to the
479 modeling of the background surface and the weakness of the signal in such conditions. Moreover, also considering
480 very low SWP and SSR values (SWP \approx 0.001 kg m⁻², SSR \approx 0.001 mm h⁻¹), HANDEL-ATMS manages to detect
481 around 60 % of the snowfall events. Similar considerations can be done also for the different background surfaces.
482 The detection capabilities are influenced both by the typical environmental conditions of each PESCA class and
483 by the uncertainties linked to the emissivity estimation. In Figure 9 the statistical scores of the algorithm
484 performance by considering each PESCA class for both the SWP and the SSR detection module are reported. It
485 can be observed that, also considering specifically the classes associated to extremely dry and cold environmental
486 conditions such as Perennial Snow or Winter Polar Snow (see *Camplani et al, 2021*), where the detection is more
487 problematic due to the uncertainties in the emissivity retrieval (see Table 2) , and to the low snowfall intensity,
488 HANDEL-ATMS has good detection capabilities (POD and FAR values greater than 0.7 and less than 0.25,
489 respectively, for both SWP and SSR). On the other hand, for surface classes characterized by the highest emission
490 estimation uncertainties, such as Deep Dry Snow, the statistical scores are coherent with the general scores and
491 better than those obtained in presence of extremely dry/cold environmental conditions. So, it is possible to
492 conclude that the extremely cold/dry environmental conditions - have more influence on the detection than the
493 uncertainties on clear sky emissivity estimation. Generally, these results provide evidence that HANDEL-ATMS
494 can be used to analyze snowfall occurrence in the polar regions.

495 The error statistics of the two estimation modules are reported in Table 5 in terms of bias, RMSE and the
496 coefficient of determination R^2 , which is defined by Equation 6.

$$497 \quad R^2 = 1 - \frac{RMSE^2}{std^2}$$

498 (6)

499 It is worth noticing that the biases are negligible for both modules while RMSE values are comparable to the light
500 events recorded in the dataset. Moreover, as expected, RMSE and R^2 values are respectively higher and lower for
501 the SSR module than for the SWP module. In Figure 10 the density scatterplots between the SWP and SSR values
502 retrieved by HANDEL-ATMS and the 2CSP corresponding values are reported. For both modules an
503 overestimation can be observed for very light snowfall (SWP < 10⁻² kg m⁻² and SSR < 10⁻² mm h⁻¹), while there
504 is a very good agreement for higher SWP and SSR values. In order to relate these results to the environmental
505 conditions, Figure 11 shows the dependence of HANDEL-ATMS snowfall estimation error statistics, as well of
506 SWP and SSR, on TPW. The curves represent, for each 1-mm TPW bin, the mean 2-CSP SWP or SSR computed,
507 the RMSE and the relative bias (the ratio between the bias and the SWP/SSR mean value for each bin). As
508 expected, TPW and snowfall intensity are strongly correlated. An increase of the absolute RMSE can be observed
509 as TPW increases, and it is larger than the SWP/SSR mean value for TPW < 8 mm. A similar behavior can be

510 observed by analyzing the dependence of HANDEL-ATMS snowfall estimation error statistics on T_{2m} (not
511 shown). A very moderate overestimation is observed for $TPW < 8$ mm and for lower SWP and SSR values ($<$
512 0.1 mm/h), with relative bias around 5%, (up to 8% only for extremely low TPW values and very low number of
513 observations (see Figure 7)), while underestimation (relative bias up to -5%) is observed for higher TPW values
514 and higher SWP and SSR values. Generally, light snowfall events are linked to the very cold/dry environmental
515 conditions typical of high-latitude regions. So, the algorithm manages to estimate also the very light SWP and
516 SSR typical of high latitudes but tends to slightly overestimate snowfall intensity in such conditions.
517 From the analysis of Figure 7-11, it can be concluded that HANDEL-ATMS has good detection capabilities (also
518 for extremely light snowfall) but it shows some limitations in correctly estimating its intensity, with slight
519 overestimation of the very light snowfall typical of high latitudes.

520

521 **4.2 A Case Study: Greenland-2016/04/24**

522 The case study reported corresponds to the observation of a moderately light snowfall event over the central part
523 of Greenland that occurred on 24 April 2016. ATMS overpass is between 14:51:23 UTC. and 14:57:47 UTC.,
524 while the CPR overpass is between 15:05:25 UTC. and 15:11:45 UTC., with a time difference of 14 minutes and
525 2 seconds. This event presents several characteristics typical of high latitudes, such as light snowfall rate, dry and
526 cold atmospheric conditions, and presence of a frozen background surface, a typical case of interest for the
527 application of HANDEL-ATMS.

528 In Figure 12 PESCA classification is reported. The entire territory of Greenland, except for a narrow area on the
529 southwestern coast, is identified as a snow-covered surface; PESCA identifies the Perennial Snow class in the
530 central part of Greenland and along CloudSat track, and the Polar Winter Snow class near the northern shoreline.
531 CloudSat overpasses the central part of the island, and CPR track is along the central part of the ATMS swath.

532 In Figure 13 a synopsis of the event along the CPR track is reported showing T_{2m} and TPW, the 2CSP SWP and
533 SSR values, the cross-section of CPR reflectivity, with the DARDAR supercooled water information
534 superimposed (in magenta). Moreover, the PESCA surface classification, and the TBs of the main ATMS high-
535 frequency channels along the CloudSat track are also shown. The event is characterized by dry conditions (TPW
536 < 5 mm) and T_{2m} below 273 K, except over the coast. CPR observes a cloud system associated to the snowfall
537 event between $68^{\circ}N$ and $76^{\circ}N$; DARDAR detects the presence of a supercooled water layer at the cloud top
538 between $68^{\circ}N$ and $72^{\circ}N$ and indicates the presence of supercooled droplets embedded in the deeper cloud
539 associated to the more intense snowfall. According to the 2CSP product, a light shallow snowfall system is found
540 in the inner part of the island while deeper, more intense snowfall, with a peak of intensity between $72^{\circ}N$ and
541 $76^{\circ}N$, is found near the shoreline. For what concerns the associated ATMS observations, an increase of the 88
542 GHz and 165 GHz TBs is observed in correspondence with the supercooled water layer, while only a slight
543 decrease of 165.5 and 183.3+7 GHz TBs can be observed in coincidence with the snowfall intensity peak.

544 In figure 12 the maps of the TB_{obs} at 165.5 GHz (top panel) and the $\Delta TB_{obs-sim}$ at 165.5 GHz (bottom panel) are
545 reported. In the top panel, it is possible to observe that, despite the snowfall event, there is not a clear TB scattering
546 signal in the area where 2CSP detects snowfall ($70^{\circ}N$ - $76^{\circ}N$, $40^{\circ}W$ - $70^{\circ}W$), instead a slight increase in the TBs
547 can be observed in the area where DARDAR detects the supercooled water layer at the cloud top. The map of
548 $\Delta TB_{obs-sim}$ allows to observe an emission signal ($\Delta TB_{obs-sim} > 0$) over the central part of the ATMS swath due to
549 the combined effect of the emission by the supercooled liquid water layers at the cloud top, as evidenced by
550 DARDAR), (evidently exceeding the scattering signal of the weak and shallow snowfall), over a radiatively cold
551 surface background. Only near the shoreline, the TB_{obs} are slightly lower than the TB_{sim} ($\Delta TB_{obs-sim} < 0$) due to
552 the stronger scattering signal of the deeper snowfall system. In Figure 15 the results of the HANDEL-ATMS four
553 modules are reported. It is worth noting that both detection modules find snowfall in the central region of
554 Greenland and near the northern coast. The estimated snowfall intensity for this event is generally low (SWP $<$
555 0.1 kg m^{-2} and SSR < 0.1 mm h^{-1}) except over the western coast, where SWP reaches 0.5 kg m^{-2} and SSR reaches
556 1 mm h^{-1} . It is worth noticing that HANDEL-ATMS detects snowfall also where there is an emission signal
557 ($\Delta TB_{obs-sim} > 0$) and that discontinuities in snowfall retrievals are not observed in correspondence with surface
558 class changes.

559 Finally, a comparison between the HANDEL-ATMS and the 2CSP is reported in Figure 16. There is a substantial
560 agreement on the snowfall detection of the two products. It can be observed that HANDEL-ATMS tends to
561 overestimate very light SWP and SSR in presence of shallow system (2CSP SWP < 0.05 kg m^{-2} and SSR < 0.1

562 mm h⁻¹, between 68°N and 72°N), consistently with what shown in Figure 10, while there is a good agreement
563 between 72°N and 76°N, where snowfall intensity increases.

564 The analysis of this case study demonstrates that the algorithm can interpret the ambiguity of the
565 emission/scattering signal often associated with snowfall events at high latitudes (as described in Section 4.1) and
566 efficiently detect, and, to a less extent, quantify snowfall even in extreme cold and dry conditions.

567 **4.3 Comparison with SLALOM-CT**

568 SLALOM-CT has been introduced in Section 1. It presents some similarities with HANDEL-ATMS: it is based
569 on an ANN approach and uses CPR-2CSP product as reference. On the other hand, substantial differences have
570 to be highlighted: SLALOM-CT was designed to operate on a global scale, while HANDEL-ATMS has been
571 developed specifically for the environmental conditions typical of high latitudes. Moreover, the predictor sets are
572 different: in addition to TB observations, SLALOM-CT relies on several model derived environmental
573 parameters, while HANDEL-ATMS relies on differences between simulated clear-sky TBs, based on the dynamic
574 estimation of the background surface emissivity (i.e., at the time of the satellite overpass), and observed TBs
575 ($\Delta T_{B_{obs-sim}}$), as described in Section 3.

576 In Table 6 a comparison between the statistical scores of the detection performances of the two algorithms is
577 reported for different environmental conditions. The comparison has been carried out considering the same
578 elements of the ATMS-CPR coincidence dataset. It can be observed that the differences between the two algorithm
579 performances increase as the environmental conditions become more extreme (i.e., lower T_{2m} and TPW), with
580 consistently better snowfall detection capabilities of HANDEL-ATMS than SLALOM-CT. Considering the
581 working limits of HANDEL-ATMS, POD increases by 2 % and FAR decreases by 8 %, while for very cold/dry
582 conditions ($T_{2m} < 250$ K, TPW < 5 mm), POD increases by 7 % and FAR decreases by 16 %; for extremely
583 dry/cold conditions ($T_{2m} < 240$ K, TPW < 3 mm), typical of the inner part of Greenland and Antarctica, POD
584 increases by 18 % and FAR decreases by 16 %.

585 **5 Conclusions and Future Perspectives**

586 In this paper a new snowfall retrieval algorithm, the High lAtitude sNow Detection and Estimation aLgorithm for
587 ATMS (HANDEL-ATMS), is described. The algorithm is based on machine learning techniques trained with
588 CPR 2CSP snowfall product and it is designed specifically for the cold and dry environmental conditions typical
589 of high latitude regions. The driving and innovative principle in the algorithm development is the exploitation of
590 the full range of ATMS channel frequencies to characterize the background surface radiative properties at the time
591 of the overpass to be able to better isolate and interpret the snowfall-related contribution to the measured multi-
592 channel upwelling radiation. A similar approach has been used by *Zhao & Weng, 2002*; however, their application
593 was limited to non-scattering surfaces and was based on empirical relationships. This approach is proven to be
594 effective for snowfall detection and quantification at high latitudes, particularly in presence of a frozen (snow-
595 covered land or sea ice) background surface, also compared to other state-of-the art machine learning based
596 methods.

597 HANDEL-ATMS can detect snowfall at high latitudes in good agreement with CPR. The estimation modules tend
598 to slightly overestimate the intensity of light snowfall events ($SWP < 10^{-2}$ kg m⁻²), with mean relative bias < 5%
599 for $SSR < 0.1$ mm/h, but it shows good accuracy for more intense snowfall events ($SWP > 10^{-2}$ kg m⁻², $SWP < 1$
600 kg m⁻²). It is worth noting, however, that the uncertainty associated with the surface emissivity estimation in some
601 conditions affects the capabilities of HANDEL-ATMS to correctly interpret the snowfall signature. Such
602 uncertainty propagates in the RTM simulation of clear-sky TBs used as input in the algorithm. Despite these
603 limitations, it is worth noticing that the development of an algorithm capable of retrieving snowfall at high
604 latitudes with good accuracy is an important development in the climate science field. The possibility to exploit
605 the high temporal sampling of the near-polar operational satellites carrying ATMS radiometers allows to achieve
606 full coverage of the polar regions. Moreover, the future European MetOp Second Generation (MetOp-SG)
607 mission, with the launch of the Sat-A Microwave Sounder (MWS), with characteristics very similar to ATMS,
608 will soon provide additional coverage to improve global snowfall monitoring. The HANDEL-ATMS
609 methodology will be adapted to be able to exploit MWS measurements in the future. The capability to estimate
610 snowfall at high temporal resolution is ancillary to the development of a snowfall monitoring system for the high
611 latitudes and to the analysis of the snowfall climatology in these areas, with possible applications in climate change
612 studies in the polar regions.

613 Future research will address some open issues. The estimation of the surface emissivity and the simulated clear-
614 sky multi-channel TBs needs to be further improved, either by considering other predictor sets or by using a
615 different technique for the emissivity spectra definition including a more advanced RTM. Another important
616 aspect is the quantification of the error linked to the background surface emissivity estimation on the snowfall
617 detection capabilities. This would be also useful for the development of modules for mountainous areas, which
618 have not been considered in the current version of the algorithm. Moreover, the effect on the algorithm snowfall
619 detection capabilities of the uncertainties linked to the model-derived environmental variables (e.g., temperature
620 and water vapor profile), which are used in the clear-sky TB simulations, should be investigated. The use of the
621 ATMS water vapor (183 GHz band) and temperature (50 GHz band) sounding channels to characterize the
622 atmospheric conditions at the time of the overpass in order to complement or avoid the use of model-derived data
623 is another subject of future research. Moreover, the development of a separate supercooled liquid water detection
624 module will be also evaluated, similarly to what is done in other PMW snowfall detection and estimation
625 algorithms (Rysman *et al*, 2018, Sandò *et al*, 2022). Such information can be exploited to improve snowfall
626 detection and estimation capabilities since the emission by the cloud droplets in dry conditions tends to mask the
627 snowfall scattering signal (see Panegrossi *et al*, 2017, Panegrossi *et al*, 2022), and adds larger uncertainties in the
628 CPR snowfall products used as reference (Battaglia & Panegrossi, 2021). Moreover, recent studies have
629 highlighted that TBs correlate more strongly with lagged surface precipitation (with a time lag of 30-60 min for
630 snowfall) than the simultaneous precipitation rate (see You *et al*, 2019). Therefore, an analysis based on a
631 coincident dataset characterized by different time lags will be conducted. The results of this analysis will be
632 compared with HANDEL-ATMS performances in order to identify a way to exploit this information towards the
633 improvement of SSR detection and estimation. Finally, since the algorithm has been developed only for specific
634 environmental conditions typical mostly of high latitudes an integration with other approaches, such as SLALOM-
635 CT, designed for global estimation of snowfall, could be considered in the future to improve global snowfall
636 monitoring based on ATMS and on future cross-track scanning radiometers.

637

638 **Data availability**

639 ATMS data are provided by the NOAA CLASS facility www.avl.class.noaa.gov/ (last access 4 april 2023), CPR
640 data are distributed by the CloudSat data processing center <https://www.cloudsat.cira.colostate.edu/> (last access
641 4 april 2023), DARDAR data are available from the ICARE FTP server of the University of Lille ([ftp.icare.univ-
642 lille1.fr](ftp.icare.univ-lille1.fr), last access 4 april 2023) and ECMWF operational forecasts are distributed by ECMWF through the
643 MARS facility via the ECGATE cluster. AutoSnow data are provided by the NOAA Satellite and Information
644 Service https://satepsanone.nesdis.noaa.gov/northern_hemisphere_multisensor.html (last access 4 april 2023).

645 **Author Contribution**

646 Conceptualization, A.C., P.S., D.C.; methodology, A.C., P.S., D.C.; software, A.C.; validation, A.C.; formal
647 analysis, A.C.; investigation, A.C., P.S., D.C., G.P.; data curation, A.C. and D.C.; writing—original draft
648 preparation, A.C.; writing—review and editing, A.C., P.S., D.C., and G.P.; visualization, A.C.; supervision, G.P.;
649 project administration, G.P.; funding acquisition, G.P. All authors have read and agreed to the published version
650 of the manuscript.

651 **Competing Interests**

652 The authors declare no conflict of interest. The funders had no role in the design of the study; in the collection,
653 analyses, or interpretation of data; in the writing of the manuscript, or in the decision to publish the results.

654 **Acknowledgements**

655 This work was carried out under the RainCast study (ESA Contract No. 4000125959/18/NL/NA) and by the
656 EUMETSAT Satellite Application Facility for Operational Hydrology and Water management (H SAF) Third and
657 Fourth Continuous and Operations Phase (CDOP-3 and CDOP-4). Andrea Camplani was supported by the Ph.D.
658 program in Infrastructures, Transport Systems and Geomatics at the Department of Civil, Constructional, and
659 Environmental Engineering at Sapienza University of Rome. The authors would like to thank EUMETSAT and
660 the NASA Precipitation Measurement Mission (PMM) Research Program for supporting scientific collaborations
661 between H SAF and GPM, and the PMM Science Team. The authors wish to express their sincere gratitude to Joe
662 Turk (NASA JPL) and Alessandro Battaglia who are warmly acknowledged for useful interactions and discussions
663 during the algorithm development and validation, and to Mattia Crespi for the scientific support to Andrea
664 Camplani during the Ph.D. program.

665 **References**

- 666 Battaglia, A., & Delanoë, J.: Synergies and complementarities of CloudSat-CALIPSO snow observations. *Journal*
667 *of Geophysical Research: Atmospheres*, 118(2), 721-731. <https://doi.org/10.1029/2012JD018092>, 2013.
- 668 Battaglia, A., & Panegrossi, G.: What can we learn from the CloudSat radiometric mode observations of snowfall
669 over the ice-free ocean?. *Remote Sensing*, 12(20), 3285, <https://doi.org/10.3390/rs12203285>, 2020.
- 670 Behrangi, A., Christensen, M., Richardson, M., Lebsock, M., Stephens, G., Huffman, G. J., Bolvin, D., Adler, R.
671 F., Gardner, A., Lambrightsten, B., & Fetzer, E.: Status of high-latitude precipitation estimates from observations
672 and reanalyses. *Journal of Geophysical Research: Atmospheres*, 121(9), 4468-4486,
673 <https://doi.org/10.1002/2015JD024546>, 2016.
- 674 Bintanja, R., Selten, F.: Future increases in Arctic precipitation linked to local evaporation and sea-ice retreat.
675 *Nature* 509, 479–482, <https://doi.org/10.1038/nature13259>, 2014.
- 676 Camplani, A., Casella, D., Sanò, P., & Panegrossi, G.: The Passive microwave Empirical cold Surface
677 Classification Algorithm (PESCA): Application to GMI and ATMS. *Journal of Hydrometeorology*, 22(7), 1727-
678 1744, <https://doi.org/10.1175/JHM-D-20-0260.1>, 2021.
- 679 Casella, D., Panegrossi, G., Sanò, P., Marra, A. C., Dietrich, S., Johnson, B. T., & Kulie, M. S.: Evaluation of the
680 GPM-DPR snowfall detection capability: Comparison with CloudSat-CPR. *Atmospheric Research*, 197, 64-75,
681 <https://doi.org/10.1016/j.atmosres.2017.06.018>, 2017.
- 682 Ceccaldi, M., Delanoë, J., Hogan, R. J., Pounder, N. L., Protat, A., & Pelon, J.: From CloudSat-CALIPSO to
683 EarthCare: Evolution of the DARDAR cloud classification and its comparison to airborne radar-lidar
684 observations. *Journal of Geophysical Research: Atmospheres*, 118(14), 7962-7981,
685 <https://doi.org/10.1002/jgrd.50579>, 2013.
- 686 DARDAR- retrieve cloud properties by combining the CloudSat radar and the CALIPSO lidar measurements.
687 CNS-CNRS-Universiteé de Lille., <https://www.icare.univ-lille.fr/dardar/>, last access: 4 April 2023.
- 688 Clifford, D.: Global estimates of snow water equivalent from passive microwave instruments: history, challenges
689 and future developments. *International Journal of Remote Sensing*, 31(14), 3707-3726,
690 <https://doi.org/10.1080/01431161.2010.483482>, 2010.
- 691 Comiso, J. C.: Sea ice effective microwave emissivities from satellite passive microwave and infrared
692 observations. *Journal of Geophysical Research: Oceans*, 88(C12), 7686-7704.
693 <https://doi.org/10.1029/JC088iC12p07686>, 1983
- 694 Cordisco, E., Prigent, C., & Aires, F.: Snow characterization at a global scale with passive microwave satellite
695 observations. *Journal of Geophysical Research: Atmospheres*, 111(D19), <https://doi.org/10.1029/2005JD006773>,
696 2006.
- 697 Fausett, L. V., Fundamentals of neural networks: architectures, algorithms and applications, Pearson Education
698 India, ISBN-13: 978-0133341867, 1994.
- 699 Felde, G. W., & Pickle, J. D.: Retrieval of 91 and 150 GHz Earth surface emissivities. *Journal of Geophysical*
700 *Research: Atmospheres*, 100(D10), 20855-20866, <https://doi.org/10.1029/95JD02221>, 1995.
- 701 Gareth, J., Daniela, W., Trevor, H., & Robert, T.: An introduction to statistical learning: with applications in R.
702 Springer, ISBN-13:978-1461471370 , 2013.
- 703 Grody, N. C., & Basist, A. N.: Global identification of snowcover using SSM/I measurements. *IEEE Transactions*
704 *on geoscience and remote sensing*, 34(1), 237-249, DOI: 10.1109/36.481908, 1996.
- 705 Hastie, T., Tibshirani, R., Friedman, J. H., & Friedman, J. H.: *The elements of statistical learning: data mining,*
706 *inference, and prediction* (Vol. 2, pp. 1-758). New York: springer, DOI: 10.1007/b94608, 2009.
- 707 Kidd, C., & Huffman, G.: Global precipitation measurement. *Meteorological Applications*, 18(3), 334-353,
708 <https://doi.org/10.1002/met.284>, 2011.
- 709 Hewison, T. J., & English, S. J.: Airborne retrievals of snow and ice surface emissivity at millimeter wavelengths.
710 *IEEE Transactions on Geoscience and Remote Sensing*, 37(4), 1871-1879, DOI: 10.1109/36.774700, 1999.
- 711 Kim, M. J., Weinman, J. A., Olson, W. S., Chang, D. E., Skofronick-Jackson, G., & Wang, J. R.: A physical
712 model to estimate snowfall over land using AMSU-B observations. *Journal of Geophysical Research:*
713 *Atmospheres*, 113(D9), <https://doi.org/10.1029/2007JD008589>, 2008.
- 714 Kohonen, T.: *Self-organization and associative memory* (Vol. 8). Springer Science & Business Media,
715 DOI:10.1007/978-3-642-88163-3, 2012.

716 Kongoli, C., Pellegrino, P., Ferraro, R. R., Grody, N. C., & Meng, H.: A new snowfall detection algorithm over
717 land using measurements from the Advanced Microwave Sounding Unit (AMSU). *Geophysical Research Letters*,
718 30(14). <https://doi.org/10.1029/2003GL017177>, 2003.

719 Kongoli, C., Meng, H., Dong, J., & Ferraro, R.: A snowfall detection algorithm over land utilizing high-frequency
720 passive microwave measurements—Application to ATMS. *Journal of Geophysical Research: Atmospheres*,
721 120(5), 1918-1932. <https://doi.org/10.1002/2014JD022427>, 2015.

722 Kongoli, C., Meng, H., Dong, J., & Ferraro, R.: A hybrid snowfall detection method from satellite passive
723 microwave measurements and global forecast weather models. *Quarterly Journal of the Royal Meteorological
724 Society*, 144, 120-132. <https://doi.org/10.1002/qj.3270>, 2018.

725 Kulie, M. S., Bennartz, R., Greenwald, T. J., Chen, Y., & Weng, F.: Uncertainties in microwave properties of
726 frozen precipitation: Implications for remote sensing and data assimilation. *Journal of the Atmospheric Sciences*,
727 67(11), 3471-3487. <https://doi.org/10.1175/2010JAS3520.1>, 2010.

728 Kulie, M. S., Milani, L., Wood, N. B., Tushaus, S. A., Bennartz, R., & L'Ecuyer, T. S.: A shallow cumuliform
729 snowfall census using spaceborne radar. *Journal of Hydrometeorology*, 17(4), 1261-1279.
730 <https://doi.org/10.1175/JHM-D-15-0123.1>, 2016.

731 Levizzani, V., Laviola, S., & Cattani, E.: Detection and measurement of snowfall from space. *Remote Sensing*,
732 3(1), 145-166. <https://doi.org/10.3390/rs3010145>, 2011.

733 Liu, Y., Key, J. R., Liu, Z., Wang, X., & Vavrus, S. J.: A cloudier Arctic expected with diminishing sea ice.
734 *Geophysical Research Letters*, 39(5). <https://doi.org/10.1029/2012GL051251>, 2012.

735 Liu, J., Curry, J. A., Wang, H., Song, M., & Horton, R. M.: Impact of declining Arctic sea ice on winter snowfall.
736 *Proceedings of the National Academy of Sciences*, 109(11), 4074-4079. <https://doi.org/10.1073/pnas.1114910109>,
737 2012.

738 Liu, G., & Seo, E. K.: Detecting snowfall over land by satellite high-frequency microwave observations: The lack
739 of scattering signature and a statistical approach. *Journal of geophysical research: atmospheres*, 118(3), 1376-
740 1387. <https://doi.org/10.1002/jgrd.50172>, 2013.

741 Mathew, N., Heygster, G., Melsheimer, C., & Kaleschke, L.: Surface emissivity of Arctic sea ice at AMSU
742 window frequencies. *IEEE transactions on geoscience and remote sensing*, 46(8), 2298-2306,
743 DOI:10.1109/TGRS.2008.916630, 2008.

744 Mätzler, C., & Hüppi, R.: Review of signature studies for microwave remote sensing of snowpacks. *Advances in
745 Space Research*, 9(1), 253-265. [https://doi.org/10.1016/0273-1177\(89\)90493-6](https://doi.org/10.1016/0273-1177(89)90493-6), 1989.

746 Meng, H., Dong, J., Ferraro, R., Yan, B., Zhao, L., Kongoli, C., Wang, N., & Zavadsky, B.: A 1DVAR-based
747 snowfall rate retrieval algorithm for passive microwave radiometers. *Journal of Geophysical Research:
748 Atmospheres*, 122(12), 6520-6540. <https://doi.org/10.1002/2016JD026325>, 2017.

749 Milani, L., Kulie, M. S., Casella, D., Dietrich, S., L'Ecuyer, T. S., Panegrossi, G., Porcù, F., Sanò, P., & Wood,
750 N. B.: CloudSat snowfall estimates over Antarctica and the Southern Ocean: An assessment of independent
751 retrieval methodologies and multi-year snowfall analysis. *Atmospheric research*, 213, 121-135,
752 <https://doi.org/10.1016/j.atmosres.2018.05.015>, 2018.

753 Milani, L., & Wood, N. B.: Biases in cloudsat falling snow estimates resulting from daylight-only operations.
754 *Remote Sensing*, 13(11), 2041. <https://doi.org/10.3390/rs13112041>, 2021.

755 Mroz, K., Montopoli, M., Battaglia, A., Panegrossi, G., Kirstetter, P., & Baldini, L.: Cross validation of active
756 and passive microwave snowfall products over the continental United States. *Journal of Hydrometeorology*, 22(5),
757 1297-1315. <https://doi.org/10.1175/JHM-D-20-0222.1>, 2021.

758 Munchak, S. J., Ringerud, S., Brucker, L., You, Y., de Gelis, I., & Prigent, C.: An active–passive microwave land
759 surface database from GPM. *IEEE Transactions on Geoscience and Remote Sensing*, 58(9), 6224-6242, DOI:
760 10.1109/TGRS.2020.2975477, 2020.

761 Noh, Y. J., Liu, G., Jones, A. S., & Vonder Haar, T. H.: Toward snowfall retrieval over land by combining satellite
762 and in situ measurements. *Journal of Geophysical Research: Atmospheres*, 114(D24),
763 <https://doi.org/10.1029/2009JD012307>, 2009.

764 Panegrossi, G., Rysman, J. F., Casella, D., Marra, A. C., Sanò, P., & Kulie, M. S.: CloudSat-based assessment of
765 GPM Microwave Imager snowfall observation capabilities. *Remote Sensing*, 9(12), 1263,
766 <https://doi.org/10.3390/rs9121263>, 2017.

767 Panegrossi, G., Casella, D., Sanò, P., Camplani, A., & Battaglia, A.: Recent advances and challenges in satellite-
768 based snowfall detection and estimation. *Precipitation Science*, 333-376, [https://doi.org/10.1016/B978-0-12-](https://doi.org/10.1016/B978-0-12-822973-6.00015-9)
769 [822973-6.00015-9](https://doi.org/10.1016/B978-0-12-822973-6.00015-9), 2022.

770 Partain, P.: CloudSat ECMWF-AUX Auxiliary Data Product Process Description and Interface Control
771 Document, Product Version P1_R05, NASA JPL CloudSat project document revision 0, pp. 16, Available from:
772 [https://www.cloudsat.cira.colostate.edu/cloudsat-static/info/dl/ecmwf-aux/ECMWF-](https://www.cloudsat.cira.colostate.edu/cloudsat-static/info/dl/ecmwf-aux/ECMWF-AUX.PDICD.P1_R05.rev0.pdf)
773 [AUX.PDICD.P1_R05.rev0.pdf](https://www.cloudsat.cira.colostate.edu/cloudsat-static/info/dl/ecmwf-aux/ECMWF-AUX.PDICD.P1_R05.rev0.pdf), 2022

774 Prigent, C., Wigneron, J. P., Rossow, W. B., & Pardo-Carrion, J. R.: Frequency and angular variations of land
775 surface microwave emissivities: Can we estimate SSM/T and AMSU emissivities from SSM/I emissivities?. *IEEE*
776 *transactions on geoscience and remote sensing*, 38(5), 2373-2386, DOI:10.1109/36.868893, 2000.

777 Prigent, C., Aires, F., Rossow, W., & Matthews, E.: Joint characterization of vegetation by satellite observations
778 from visible to microwave wavelengths: A sensitivity analysis. *Journal of Geophysical Research: Atmospheres*,
779 106(D18), 20665-20685, <https://doi.org/10.1029/2000JD900801>, 2001.

780 Prigent, C., Jaumouille, E., Chevallier, F., & Aires, F.: A parameterization of the microwave land surface
781 emissivity between 19 and 100 GHz, anchored to satellite-derived estimates. *IEEE Transactions on Geoscience*
782 *and Remote Sensing*, 46(2), 344-352, DOI: 10.1109/TGRS.2007.908881, 2008.

783 Prigent, C., Aires, F., Wang, D., Fox, S., & Harlow, C.: Sea-surface emissivity parametrization from microwaves
784 to millimetre waves. *Quarterly Journal of the Royal Meteorological Society*, 143(702), 596-605.
785 <https://doi.org/10.1002/qj.2953>, 2017.

786 Rahimi, R., Ebtehaj, A., Panegrossi, G., Milani, L., Ringerud, S. E., & Turk, F. J., Vulnerability of Passive
787 Microwave Snowfall Retrievals to Physical Properties of Snowpack: A Perspective From Dense Media Radiative
788 Transfer Theory. *IEEE Transactions on Geoscience and Remote Sensing*, 60, 1-13,
789 <https://doi.org/10.3390/rs11192200>, 2017.

790 Romanov, P.: Global multisensor automated satellite-based snow and ice mapping system (GMASI) for
791 cryosphere monitoring. *Remote Sensing of Environment*, 196, 42-55, <https://doi.org/10.1016/j.rse.2017.04.023>,
792 2017.

793 Rosenkranz, P. W., Water vapor microwave continuum absorption: A comparison of measurements and models.
794 *Radio Science*, 33(4), 919-928. <https://doi.org/10.1029/98RS01182>, 1998.

795 Rysman, J. F., Panegrossi, G., Sanò, P., Marra, A. C., Dietrich, S., Milani, L., & Kulie, M. S.: SLALOM: An all-
796 surface snow water path retrieval algorithm for the GPM Microwave Imager. *Remote Sensing*, 10(8), 1278,
797 <https://doi.org/10.3390/rs10081278>, 2018.

798 Rysman, J. F., Panegrossi, G., Sano, P., Marra, A. C., Dietrich, S., Milani, L., Kulie, M. S., Casella, D., Camplani,
799 A., Claud, C., & Edel, L.: Retrieving surface snowfall with the GPM Microwave Imager: A new module for the
800 SLALOM algorithm. *Geophysical Research Letters*, 46(22), 13593-13601,
801 <https://doi.org/10.1029/2019GL084576>, 2019.

802 Sanò, P., Casella, D., Camplani, A., D'Adderio, L. P., & Panegrossi, G., A Machine Learning Snowfall Retrieval
803 Algorithm for ATMS. *Remote Sensing*, 14(6), 1467, <https://doi.org/10.3390/rs14061467>, 2022.

804 Sanò, P., Panegrossi, G., Casella, D., Di Paola, F., Milani, L., Mugnai, A., Petracca, M., & Dietrich, S. (2015).
805 The Passive microwave Neural network Precipitation Retrieval (PNPR) algorithm for AMSU/MHS observations:
806 description and application to European case studies. *Atmospheric Measurement Techniques*, 8(2), 837-857,
807 <https://doi.org/10.5194/amt-8-837-2015>, 2015.

808 Skofronick-Jackson, G. M., Kim, M. J., Weinman, J. A., & Chang, D. E. (2004). A physical model to determine
809 snowfall over land by microwave radiometry. *IEEE Transactions on Geoscience and Remote Sensing*, 42(5),
810 1047-1058, DOI:10.1109/TGRS.2004.825585, 2004.

811 Skofronick-Jackson, G., Hudak, D., Petersen, W., Nesbitt, S. W., Chandrasekar, V., Durden, S., Kristin, J. G.,
812 Huang, G., Joe, P., Kollias, P., Reed, K., A., Schwaller, M., R., Stewart, R., Tanelli, S., Tokay, A., Wang, J., R.,
813 & Wolde, M.: Global precipitation measurement cold season precipitation experiment (GCPEX): For
814 measurement's sake, let it snow. *Bulletin of the American Meteorological Society*, 96(10), 1719-1741,
815 <https://doi.org/10.1175/BAMS-D-13-00262.1>, 2015.

816 Stephens, G. L., Vane, D. G., Tanelli, S., Im, E., Durden, S., Rokey, M., Reinke, D., Partain, P., Mace, G. G.,
817 Austin, R., L'Ecuyer, T., Haynes, J., Lebsock, M., Suzuki, K., Waliser, D., Wu, D., Kay, J., Gettelman, A., Zhi

818 Wang, Z., & Marchand, R.: CloudSat mission: Performance and early science after the first year of operation.
819 *Journal of Geophysical Research: Atmospheres*, 113(D8), <https://doi.org/10.1029/2008JD009982>, 2008.

820 Takbiri, Z., Ebtehaj, A., Foufoula-Georgiou, E., Kirstetter, P. E., & Turk, F. J.: A prognostic nested k-nearest
821 approach for microwave precipitation phase detection over snow cover. *Journal of hydrometeorology*, 20(2), 251-
822 274, <https://doi.org/10.1175/JHM-D-18-0021.1>, 2019.

823 Turk, F. J., Ringerud, S. E., Camplani, A., Casella, D., Chase, R. J., Ebtehaj, A., Gong, J., Kulie, M., Liu, G.,
824 Milani, L., Panegrossi, G., Padullés, R., Rysman, J. F., Sanò, P., Vahedizade, S., & Wood, N. B.: Applications of
825 a CloudSat-TRMM and CloudSat-GPM satellite coincidence dataset. *Remote Sensing*, 13(12), 2264,
826 <https://doi.org/10.3390/rs13122264>, 2021a.

827 Turk, F. J., Ringerud, S. E., You, Y., Camplani, A., Casella, D., Panegrossi, G., Sanò, P., Ebtehaj, A., Guilloteau,
828 C., Utsumi, N., Prigent, C., & Peters-Lidard, C.: Adapting passive microwave-based precipitation algorithms to
829 variable microwave land surface emissivity to improve precipitation estimation from the GPM constellation.
830 *Journal of Hydrometeorology*, 22(7), 1755-1781, <https://doi.org/10.1175/JHM-D-20-0296.1>, 2021.

831 Ulaby, F., & Long, D., Microwave radar and radiometric remote sensing, 1st Edition, the Univ. of Michigan Press,
832 ISBN: 978-0-472-11935-6, 2014.

833 Vihma, T., Screen, J., Tjernström, M., Newton, B., Zhang, X., Popova, V., Deser, C., Holland, M., & Prowse, T.:
834 The atmospheric role in the Arctic water cycle: A review on processes, past and future changes, and their impacts.
835 *Journal of Geophysical Research: Biogeosciences*, 121(3), 586-620, <https://doi.org/10.1002/2015JG003132>,
836 2016.

837 Wang, Y., Liu, G., Seo, E. K., & Fu, Y.: Liquid water in snowing clouds: Implications for satellite remote sensing
838 of snowfall. *Atmospheric research*, 131, 60-72, <https://doi.org/10.1016/j.atmosres.2012.06.008>, 2013.

839 Weng, F., Zou, X., Wang, X., Yang, S., & Goldberg, M. D.: Introduction to Suomi national polar-orbiting
840 partnership advanced technology microwave sounder for numerical weather prediction and tropical cyclone
841 applications. *Journal of geophysical research: atmospheres*, 117(D19), <https://doi.org/10.1029/2012JD018144>,
842 2012.

843 Wood, N. B. and T. S. L'Ecuyer: Level 2C Snow Profile Process Description and Interface Control Document,
844 Product Version P1 R05. NASA JPL CloudSat project document revision 0., 26 pp, Available from
845 [https://www.cloudsat.cira.colostate.edu/cloudsat-static/info/dl/2c-snow-profile/2C-SNOW-
846 PROFILE_PDICD.P1_R05.rev0_.pdf](https://www.cloudsat.cira.colostate.edu/cloudsat-static/info/dl/2c-snow-profile/2C-SNOW-PROFILE_PDICD.P1_R05.rev0_.pdf), 2018.

847 You, Y., Meng, H., Dong, J., Fan, Y., Ferraro, R. R., Gu, G., & Wang, L.: A Snowfall Detection Algorithm for
848 ATMS Over Ocean, Sea Ice, and Coast. *IEEE Journal of Selected Topics in Applied Earth Observations and
849 Remote Sensing*, 15, 1411-1420, DOI: [10.1109/JSTARS.2022.3140768](https://doi.org/10.1109/JSTARS.2022.3140768), 2022.

850 You, Y., Meng, H., Dong, J., & Rudlosky, S.: Time-lag correlation between passive microwave measurements
851 and surface precipitation and its impact on precipitation retrieval evaluation. *Geophysical Research Letters*,
852 46(14), 8415-8423, doi: 10.1029/2019GL083426, 2019.

853 Zhao, L., & Weng, F.: Retrieval of ice cloud parameters using the Advanced Microwave Sounding Unit. *Journal
854 of Applied Meteorology and Climatology*, 41(4), 384-395, <https://www.jstor.org/stable/26184983>, 2002.

855
856
857
858
859
860
861
862
863
864
865
866
867
868
869

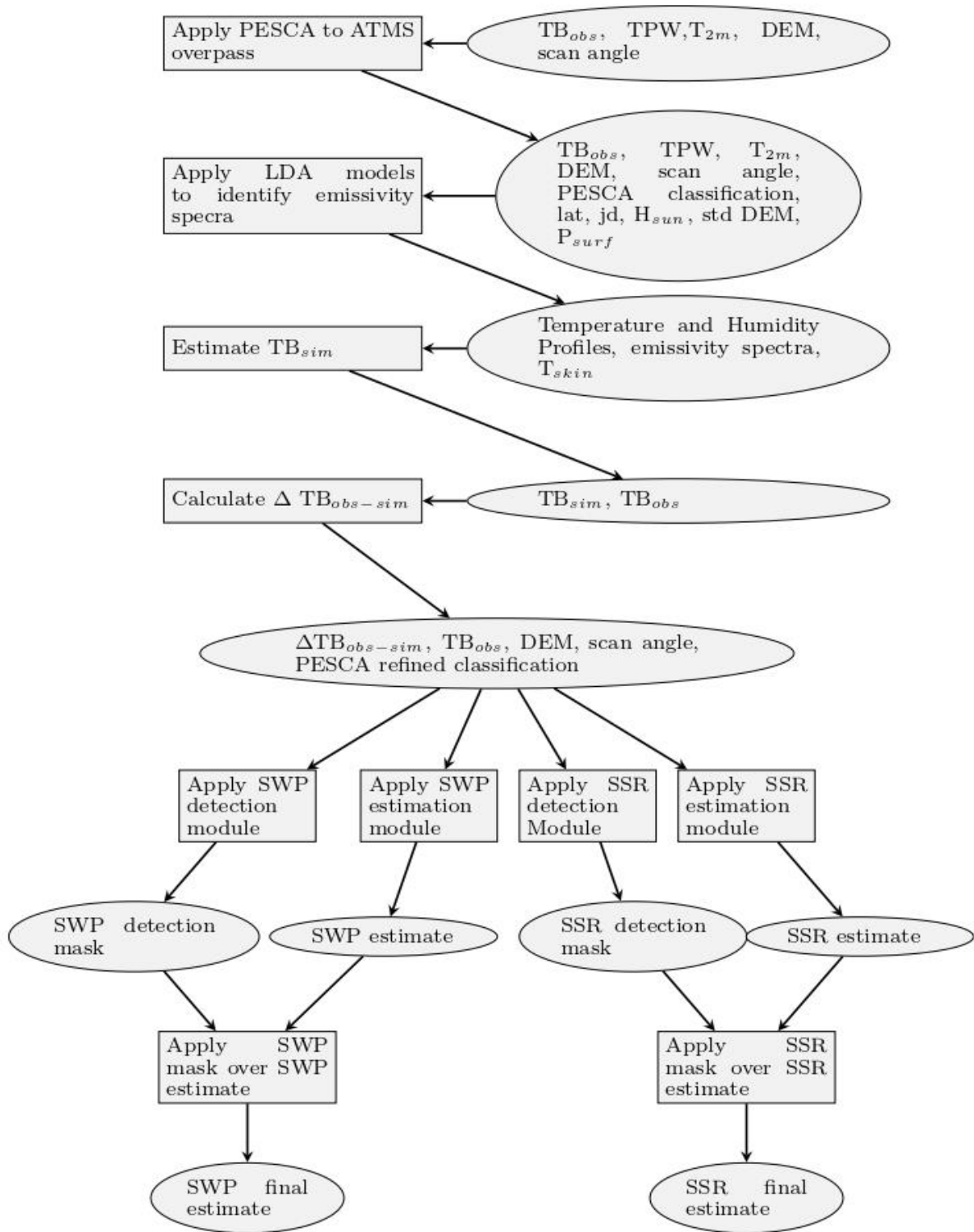
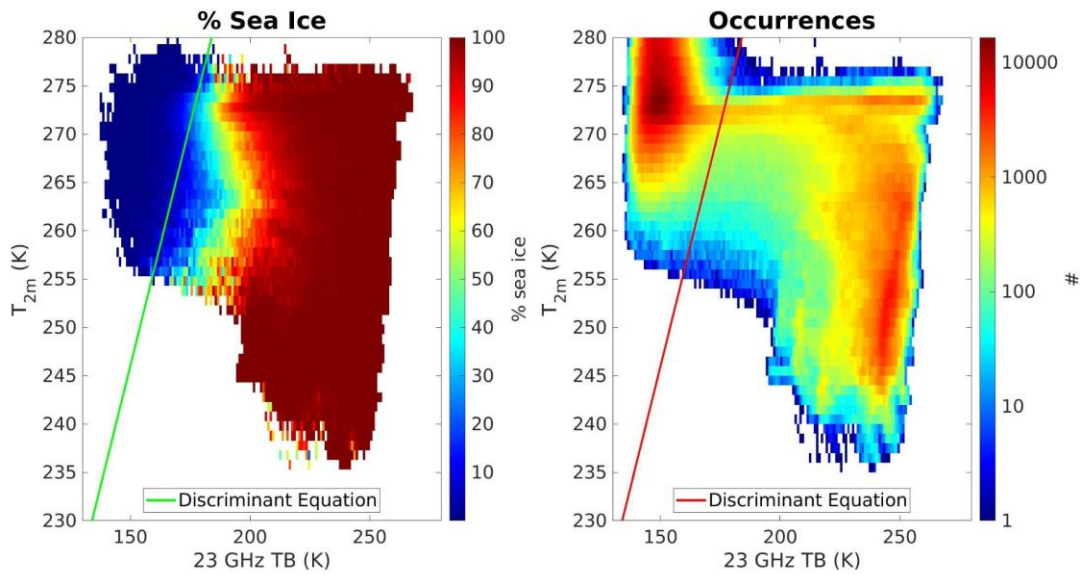


Figure 1: HANDEL-ATMS workflow diagram (please, refer to the text for details)

871
872
873



874
875
876
877
878

Figure 2: Sea Ice detection representation on a 23 TB- T_{2m} Plane. The color represents the mean AutoSnow sea ice percentage within each bin (left) and the observation occurrence (right). The green (left) and red (right) lines represent the discriminant Equation (Equation 1) between sea ice and ocean.

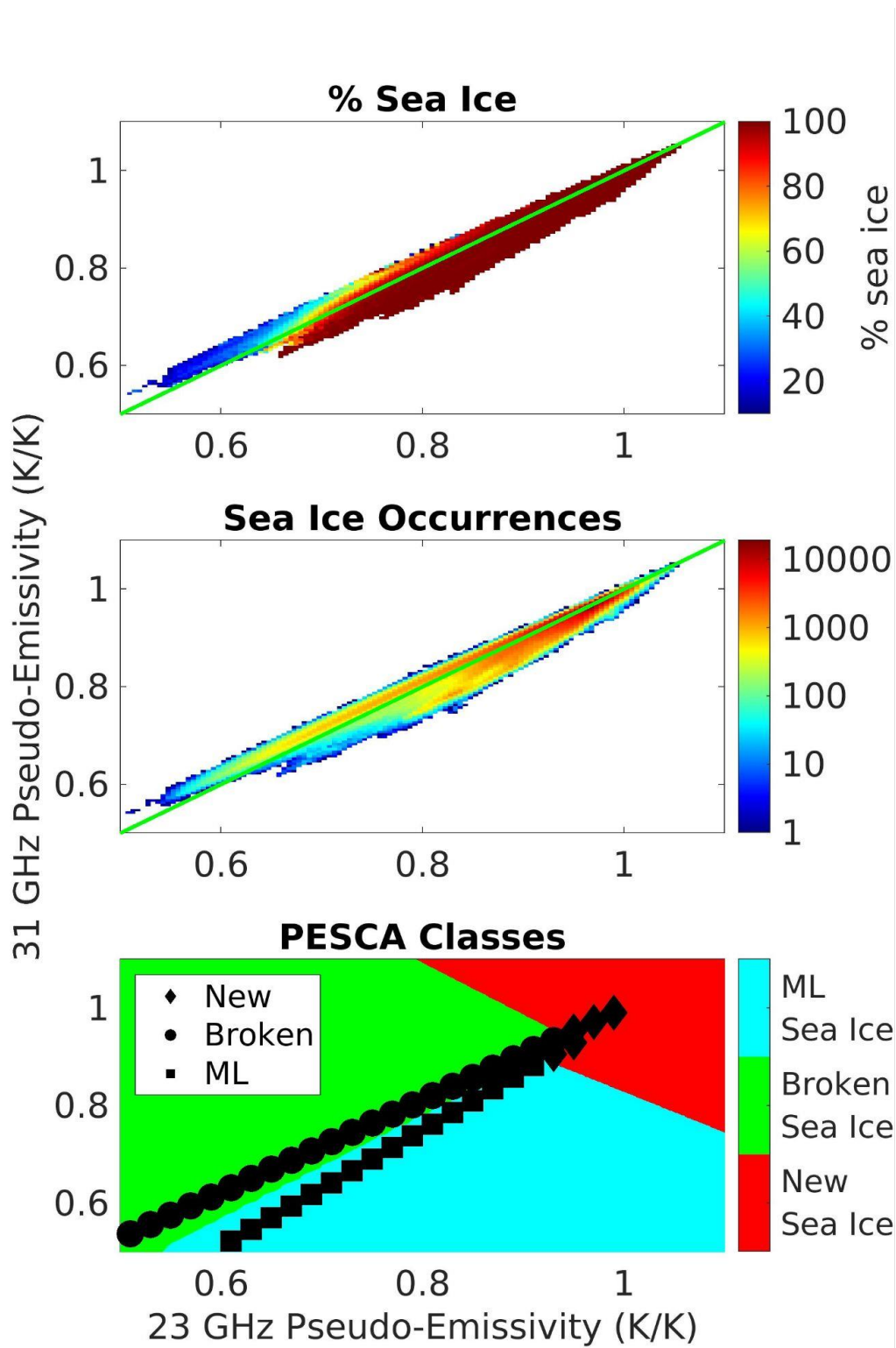
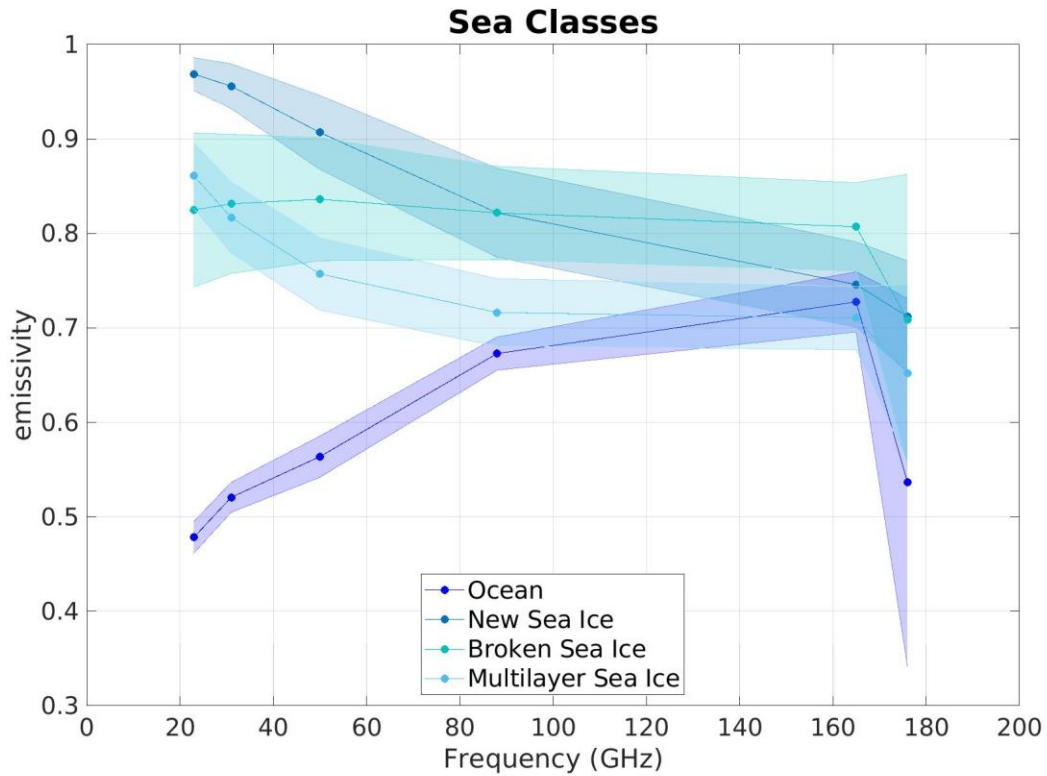


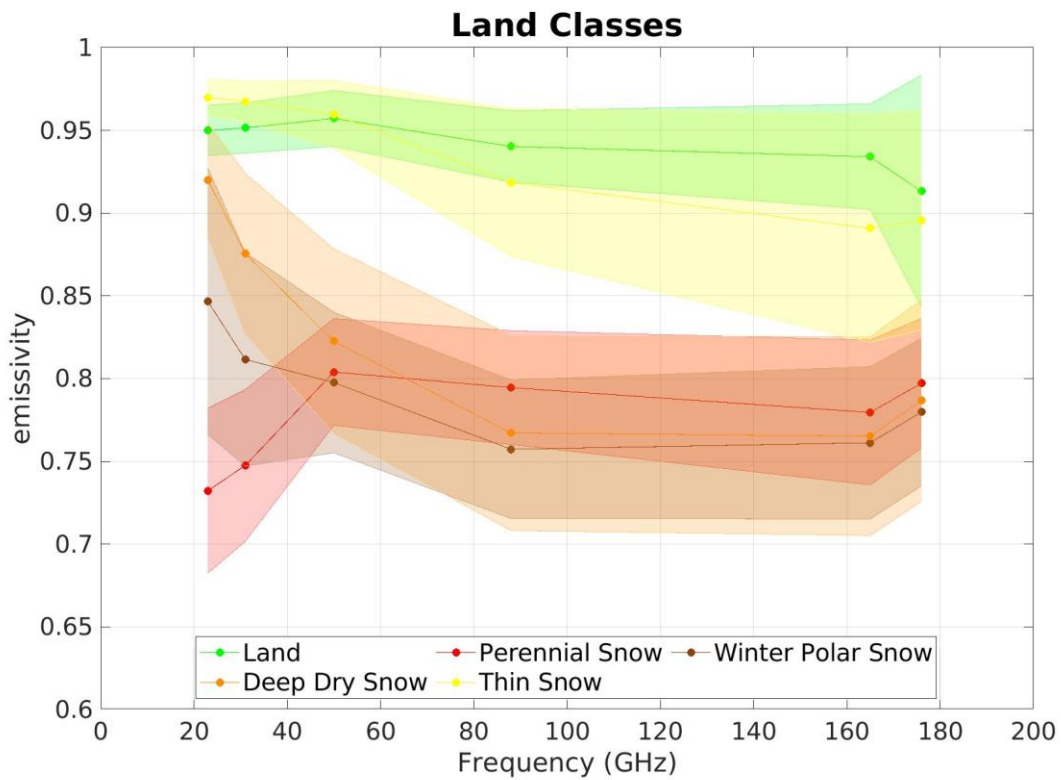
Figure 3: Sea Ice detection and classification: relationship between 31 GHz Pseudo-Emissivity (y-axis) and 23 GHz Pseudo-Emissivity (x-axis). The color represents the mean AutoSnow sea ice percentage within each bin (top panel), the observation occurrence (middle panel), and the PESCA classification (Multi-Layer (ML), Broken and New sea ice) with the Nearest Neighbor markers (bottom panel).

879
880
881
882
883
884



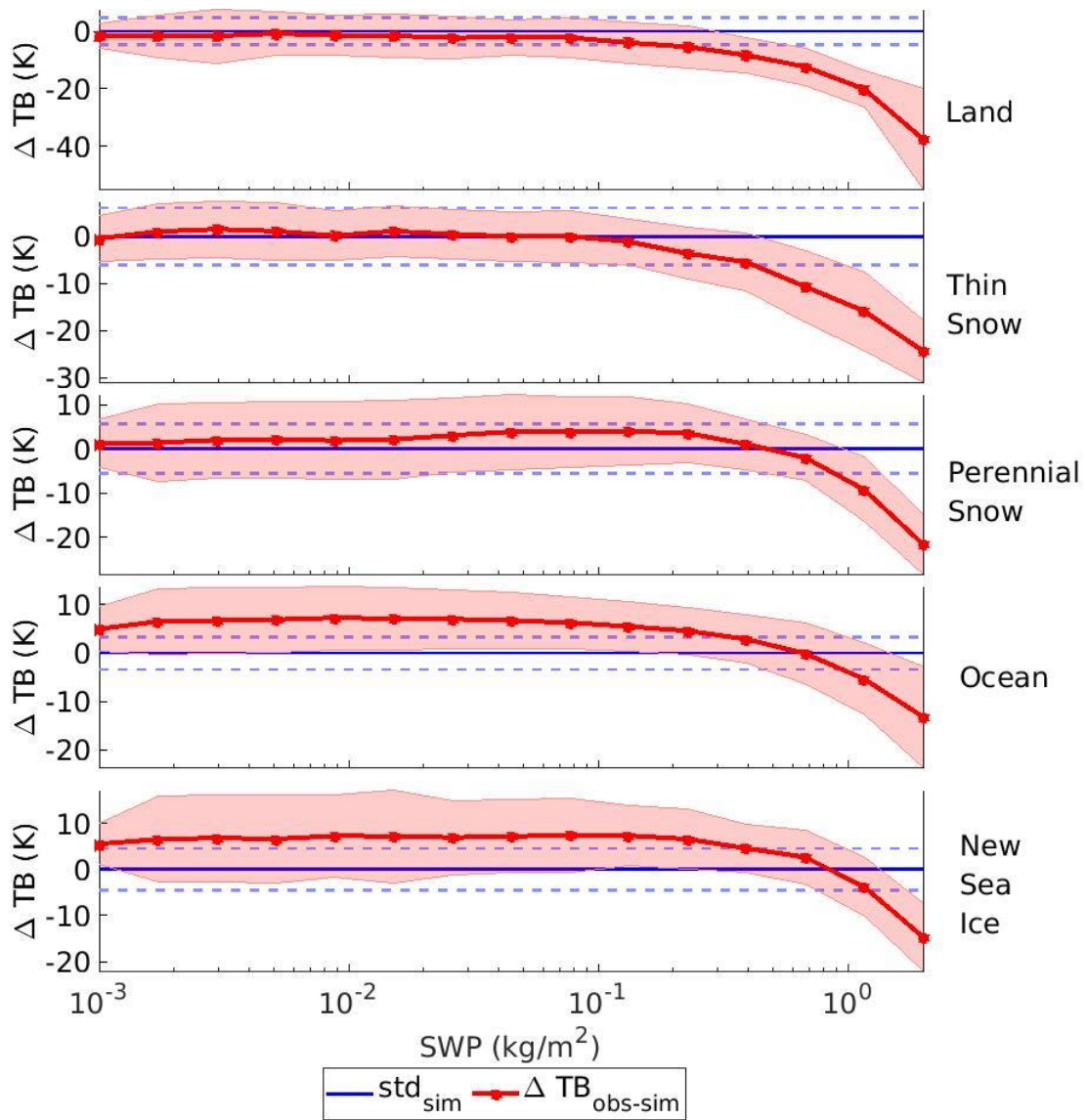
885
886
887
888

Figure 4: Emissivity Spectra for PESCA Sea Classes. The continuous lines represent the mean values of the emissivity while the shaded areas represent the standard deviation calculated at the ATMS reference frequencies (23.8 GHz, 31.4 GHz, 50.3 GHz, 88.2 GHz, 165.5 GHz, and 183.3 ±7 GHz) represented by the dots.



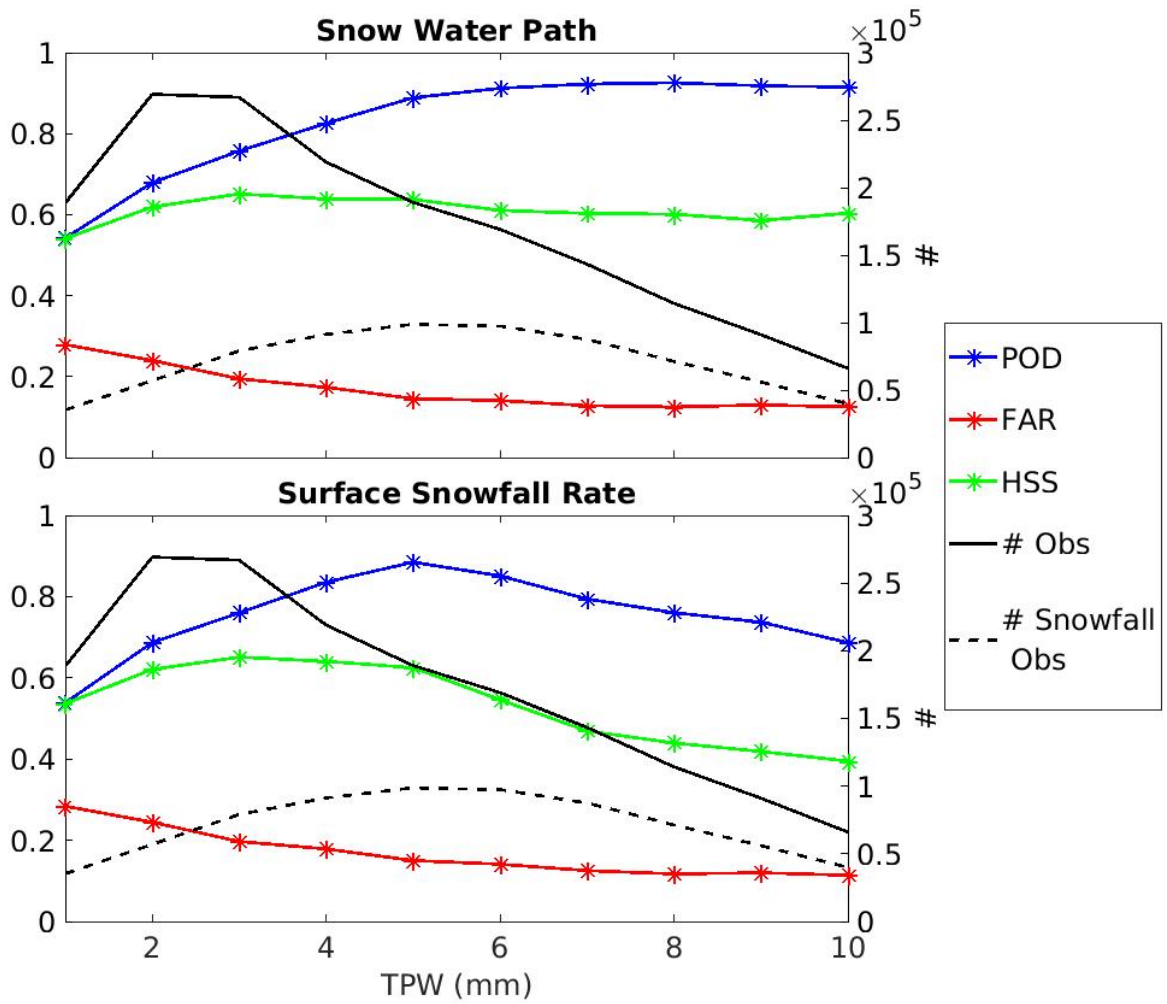
889
890

Figure 5: Same as Figure 4 but for PESCA Land Classes.



891
 892
 893
 894
 895

Figure 6: Snowfall Signature at 165.5 GHz as a function of SWP for five PESCA surface classes. The red line and shaded areas represent the mean values and standard deviations of $\Delta TB_{obs-sim}$ (i.e., the snowfall signature) while the blue lines are centered on the estimated bias and standard deviation of $\Delta TB_{obs-sim}$ in clear sky conditions for the corresponding PESCA surface class.



896

897

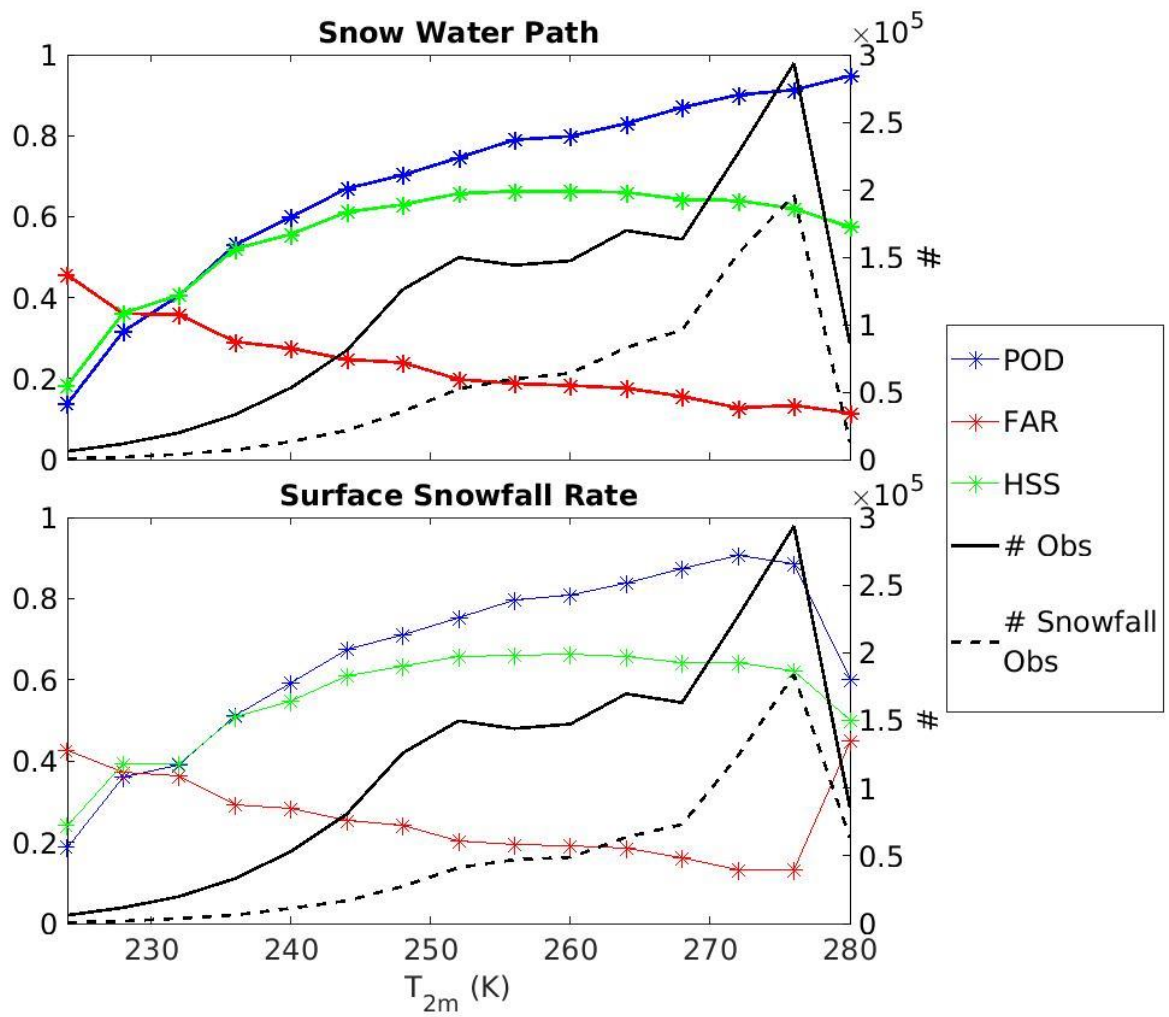
898

899

900

901

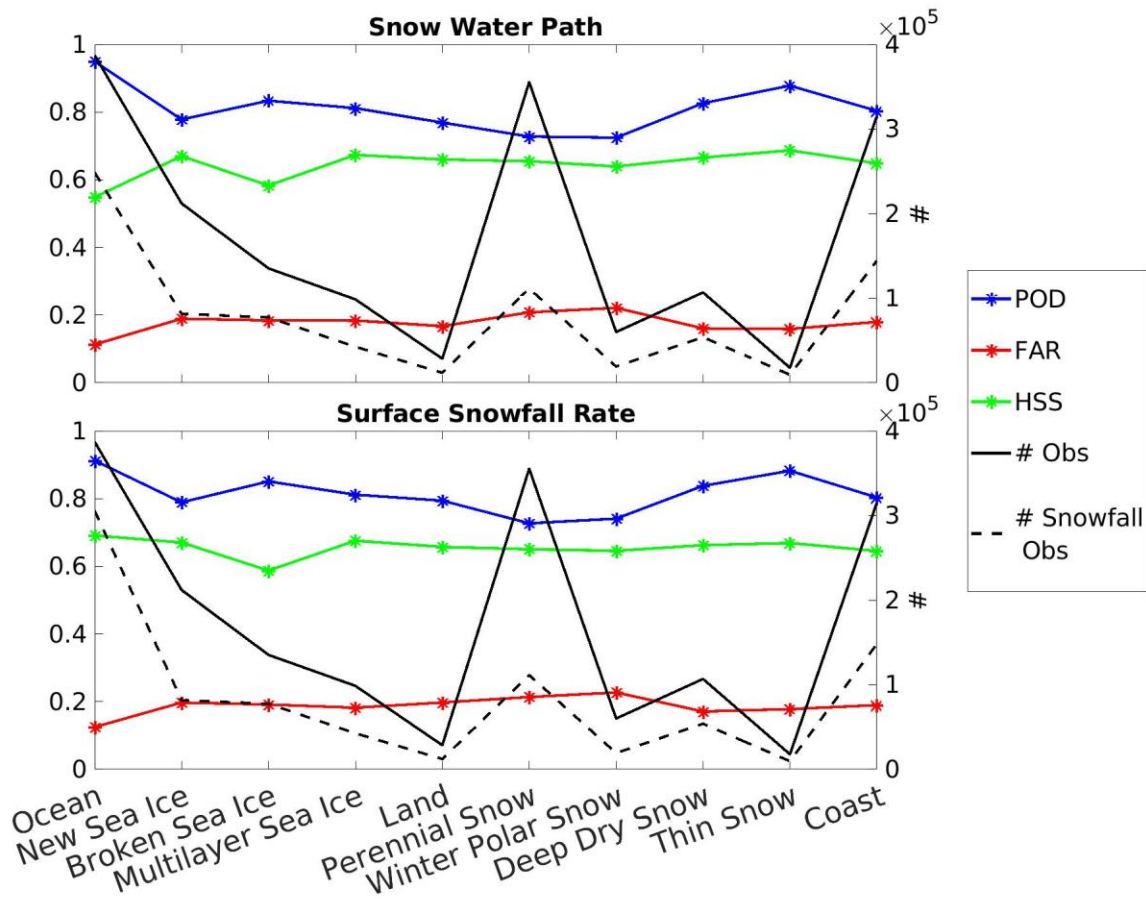
Figure 7: Dependence of HANDEL-ATMS SWP and SSR detection statistical scores on TPW. Each star represents the statistical score value for different 1-mm t bin of TPW. The left y-axis reports POD, FAR and HSS values, while the right y-axis reports the number of total and snowfall observations in the validation dataset.



902

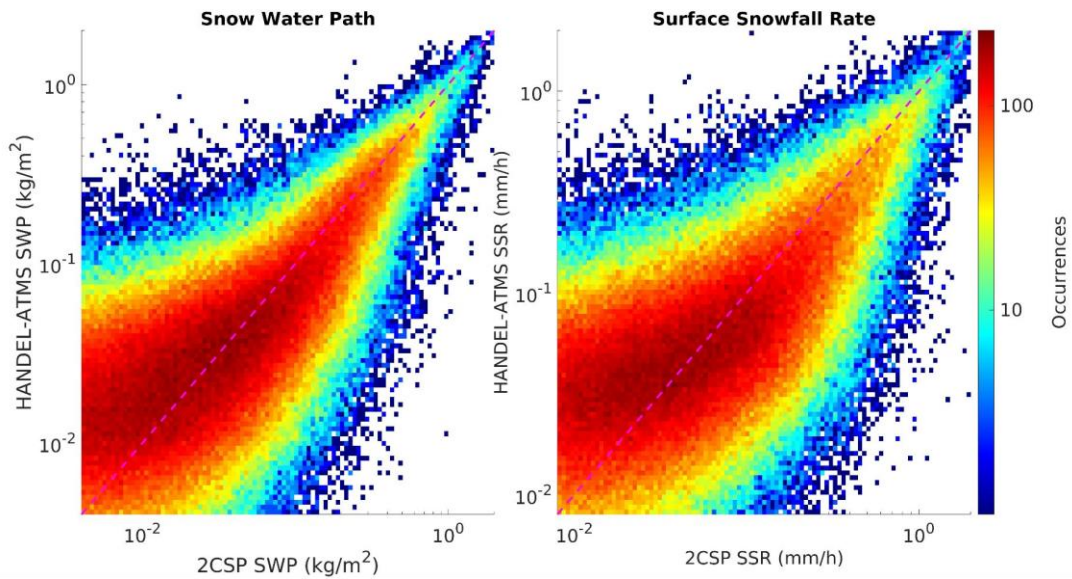
903

Figure 8: Same as Figure 7 but for T_{2m} bins.



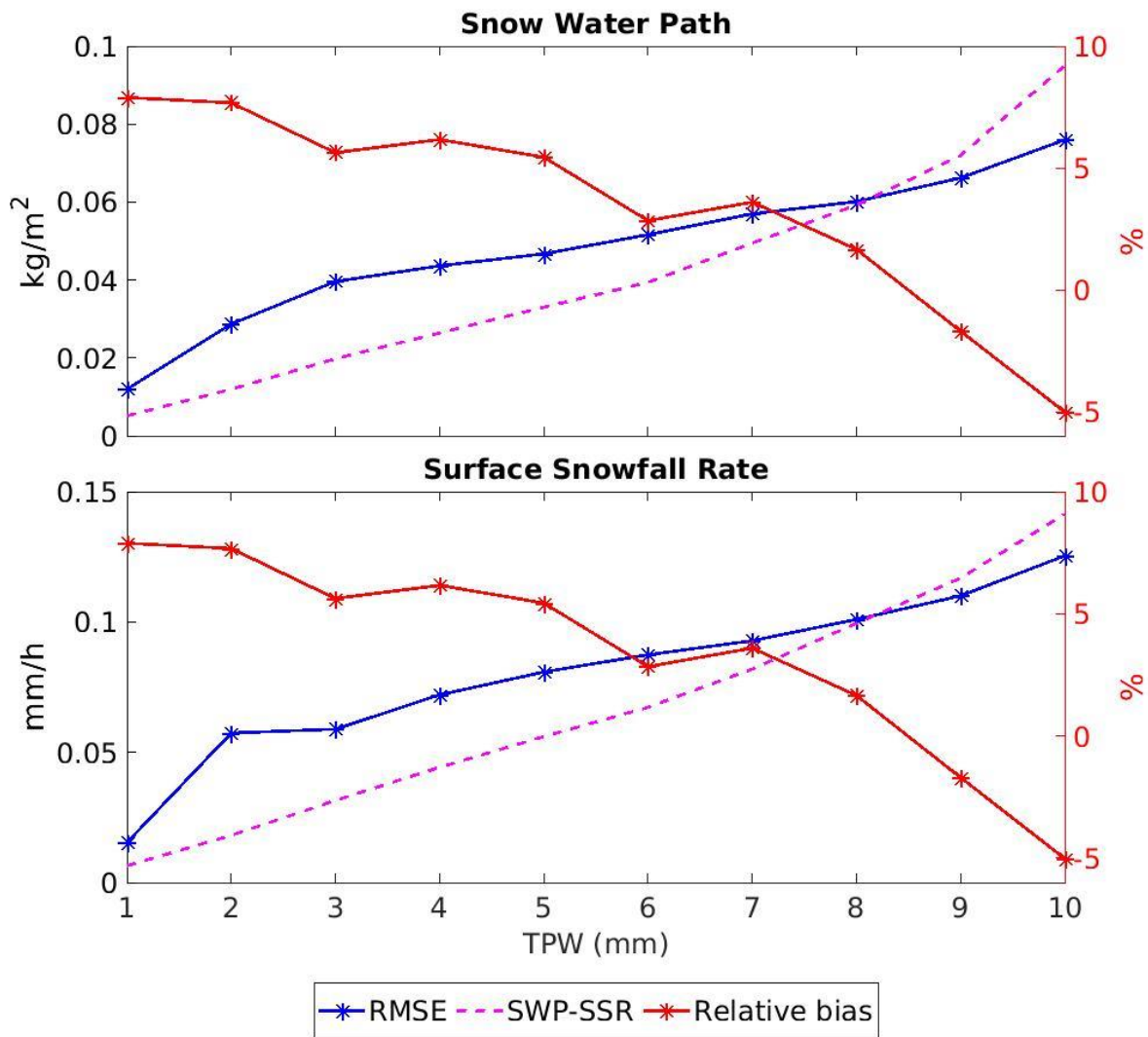
904
905
906
907

Figure 9: Same as Figure 7 but for PESCA surface classes. Each star represents the value of the statistical score for each surface category.



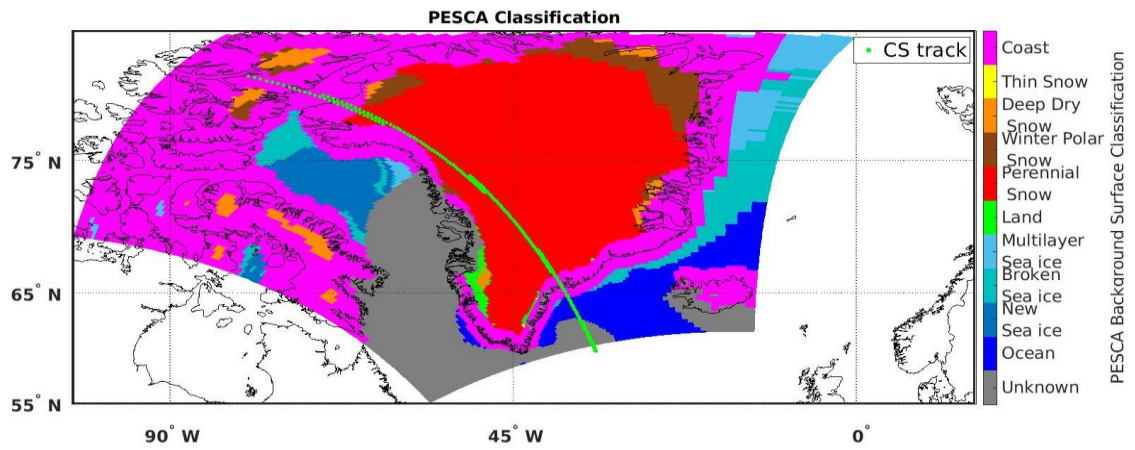
908
909
910
911
912
913

Figure 10: 2D Histogram reporting HANDDEL-ATMS SWP (left) and SSR (right) estimation (y-axis) and 2CSP estimation (x-axis). The colorbar represents the number of observations for each HANDDEL-ATMS/2CSP bin. The violet dashed line represents the bisector.



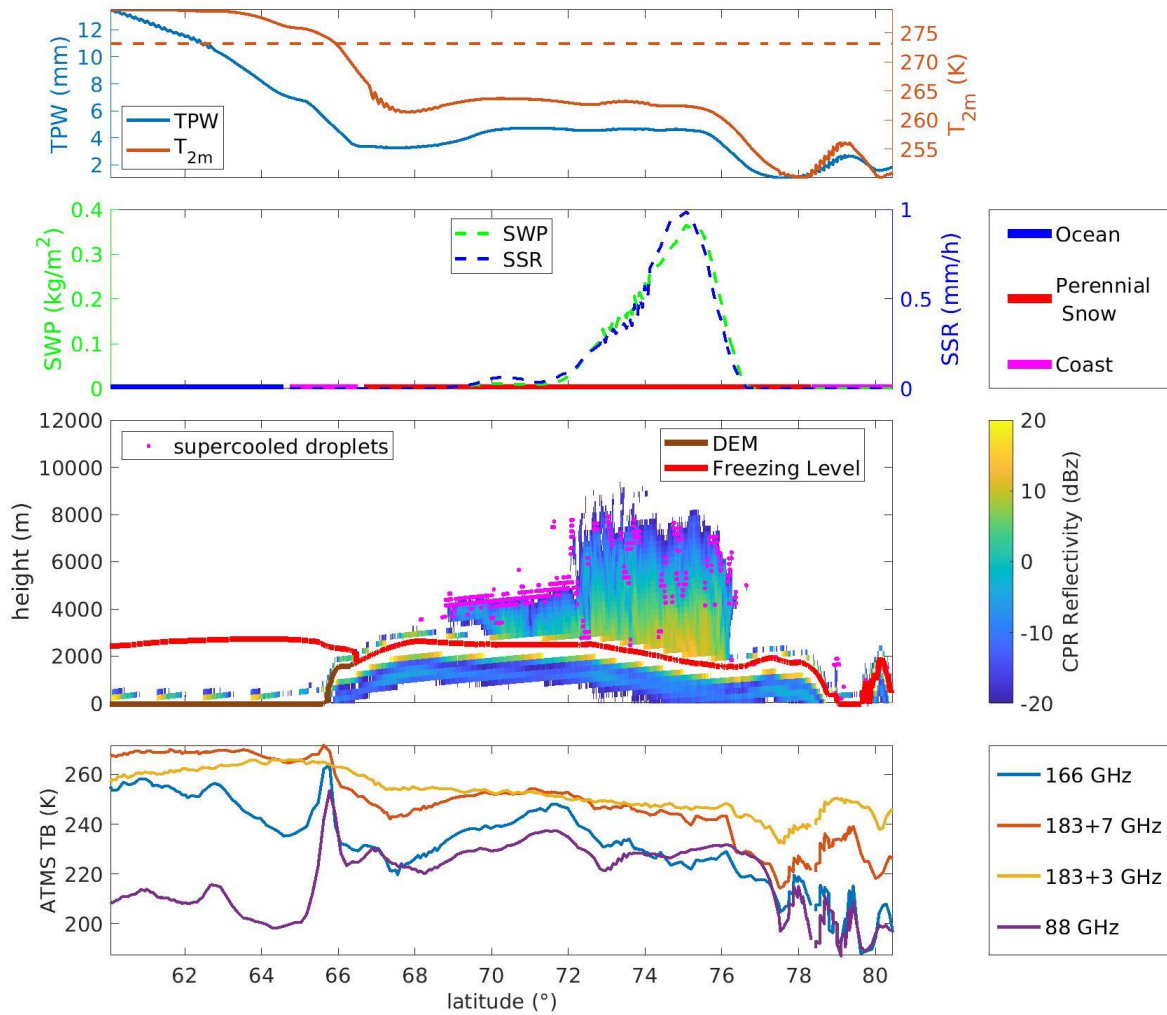
914
915
916
917
918
919

Figure 11: Dependence of HANDEL-ATMS SWP and SSR estimation on TPW. Each star represents the value of the statistical score for different 1-mm TPW bins. The left y-axis reports the RMSE and the mean intensity SWP and SSR value for each 1-mm TPW bin, while the right y-axis reports the relative bias, calculated as the ratio between the bias and the SWP/SSR mean value for each bin.



920
921
922
923
924
925

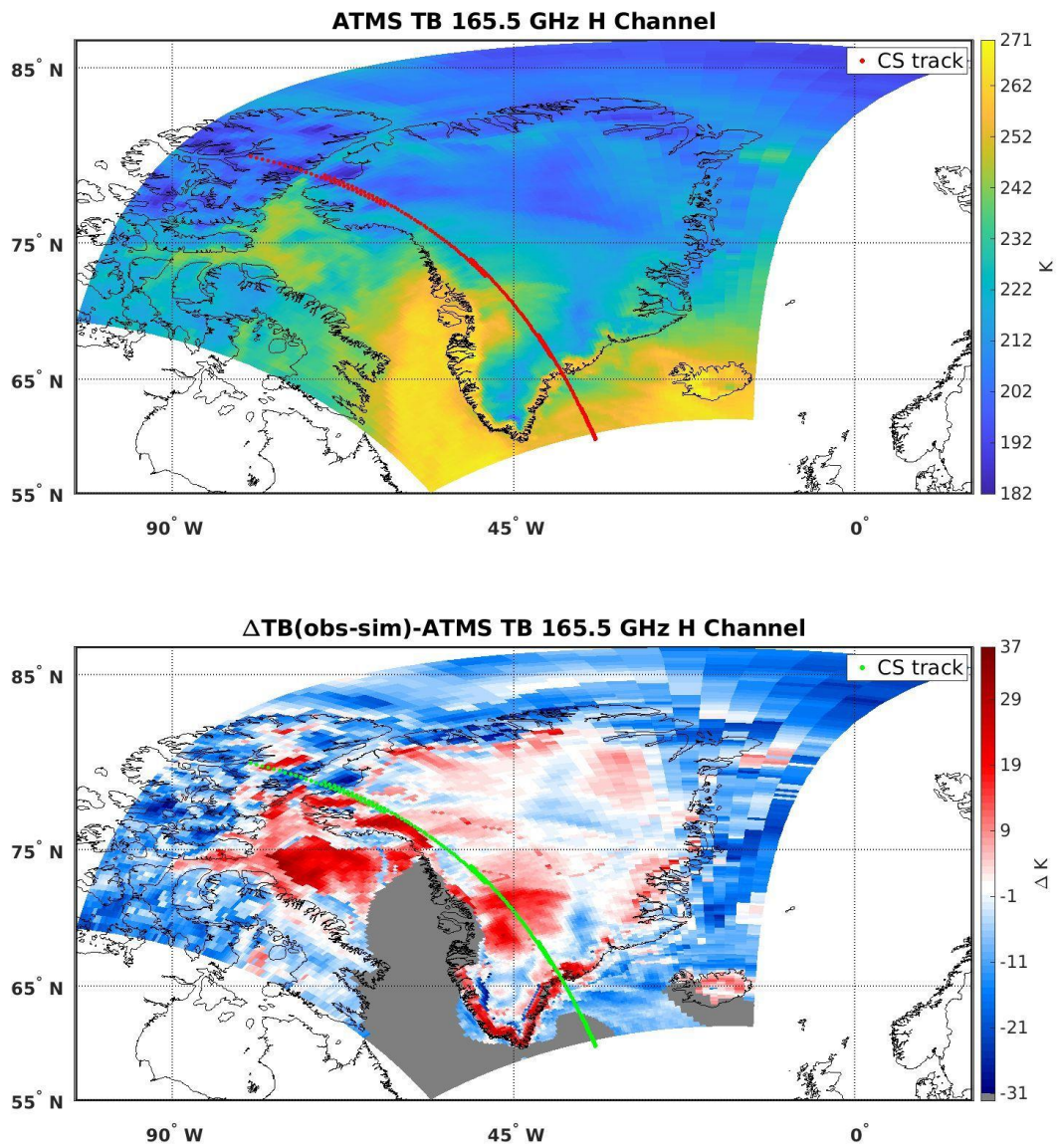
Figure 12: Greenland - 2016/04/24 - ATMS overpass is between 14:54 UTC and 14:58 UTC, while the CPR overpass is between 15:05 UTC and 15:12 UTC. Map of the PESCA Background Surface Classification. The green dotted line represents the CloudSat track.



926

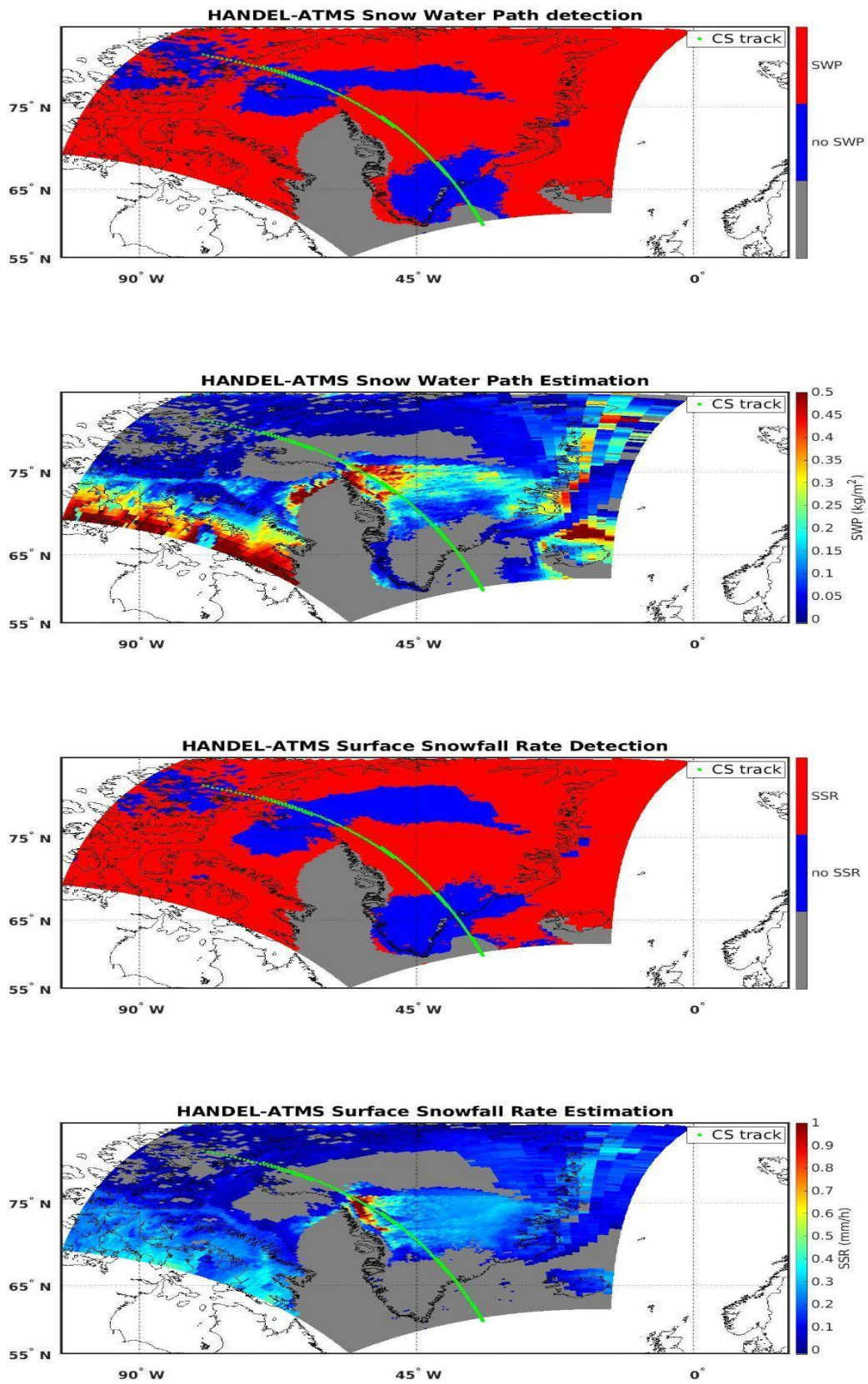
927
 928
 929
 930
 931
 932
 933
 934
 935
 936
 937
 938

Figure 13: Greenland - 2016/04/24 - Synopsis along CloudSat Track. First panel: ECMWF TPW and T_{2m} values along the CloudSat track. Second panel: the 2CSP SWP (left) and the SSR (right), and the PESCA classification along CloudSat track. Third panel: CPR reflectivity (values are reported in the colorbar on the right), and supercooled water droplets detected by DARDAR (magenta points), Digital Elevation Model (brown line) and the ECMWF Freezing Level (red line) along CloudSat track. Bottom panel: the ATMS TBs of the high-frequency channels (88 GHz, 166 GHz, 183+3 GHz, 183+7 GHz) along CloudSat track.



939
 940
 941
 942
 943
 944

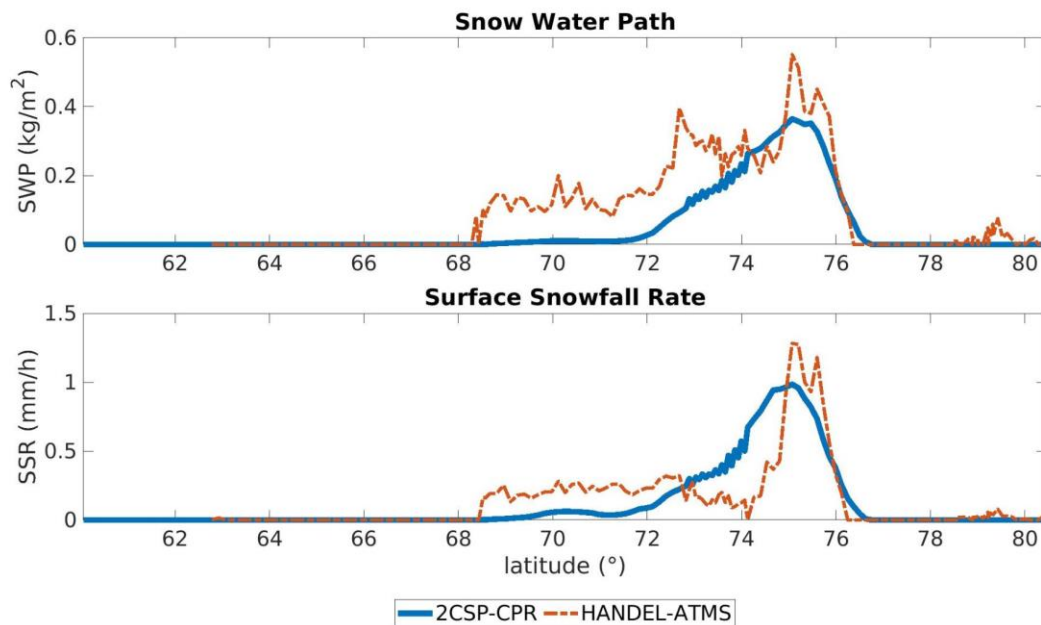
Figure 14: Greenland - 2016/04/24 - 165 GHz Channel measured TB (TB_{obs}) (top panel) and the deviation of TB_{obs} from the simulated clear-sky TBs ($\Delta TB_{\text{obs-sim}}$) (bottom panel). The red dotted line (top panel) and the green dotted line (bottom panel) represent the CloudSat track.



945
 946
 947
 948

Figure 15: Greenland - 2016/04/24 - Maps of the HANDEL-ATMS module's output: the SWP detection mask (top panel), the estimated SWP (kg m^{-2}) (second panel), the SSR detection mask (third panel), the estimated SSR (mm h^{-1}) (bottom panel). The green dotted lines (bottom panel) represent the CloudSat track.

949
950



951

952

953

Figure 16: Greenland - 2016/04/24 - Comparison between CPR 2C-SNOW-PROFILE and HANDEL-ATMS SWP and SSR estimates along the CloudSat track.

954

955

956

957

Tables

958

959

960

	OCEAN MODULE	LAND MODULE
POD	0.99	0.98
FAR	0.01	0.01
HSS	0.98	0.72

961

Table 1: PESCA Overall Statistical Scores

962

963

964

965

966

967

968

969

970

971

972

973

974

975
976

Class	n clusters	accuracy	165.5 GHz RMSE (K)	165.5 GHz NRMSE%	Predictor Set
Ocean	2	0.9	3.37	44	$P_{surf} - TPW - T_{2m}$
New Sea Ice	3	0.74	4.52	48	SI - T_{2m} - P_{surf} - ratio - jd - pem ₂₃
Broken Sea Ice	16	0.56	5.34	41	pem ₂₃ - TPW - SI - P_{surf}
Multilayer Sea Ice	9	0.53	4.38	34	pem ₃₁ - SI - TPW - T_{2m} - pem ₂₃ - P_{surf}
Land	2	0.87	4.57	52	DEM - jd - TPW
Perennial Snow	8	0.65	5.98	54	pem ₂₃ - jd - SI - pem ₃₁ - lat
Winter Polar Snow	5	0.76	5.87	37	pem ₃₁ -SI - lat - H_{sol} - pem ₃₁ - jd
Deep Dry Snow	15	0.34	6.77	45	SI - pem ₃₁ - ratio
Thin Snow	3	0.78	6.03	39	SI -ratio - lat
Coast	13	0.43	6.80	44	SI - pem ₂₃ - pem ₃₁ - DEM - T_{2m}

977 **Table 2: Classification Refinement - Parameters.**
978

Predictor Set	POD	FAR	HSS
$\Delta TB_{obs-sim}$ + ancillary parameters	0.75	0.29	0.48
TB_{obs} + ancillary parameters	0.81	0.18	0.65
TB_{obs} +environmental var+ ancillary parameters	0.82	0.17	0.68
$TB_{obs}+\Delta TB_{obs-sim}$ + ancillary parameters	0.84	0.16	0.69

979 **Table 3: HANDEL-ATMS SSR Detection Performance: Statistical scores for different Predictor Sets**
980

	POD	FAR	HSS
SWP	0.85	0.15	0.70
SSR	0.84	0.16	0.69

981 **Table 4: HANDEL-ATMS detection Performance - SWP and SSR Detection Modules Statistical Scores**
982

	RMSE	bias	R ²
SWP (kg m ⁻²)	0.047	0.001	0.72
SSR (mm h ⁻¹)	0.079	0.002	0.61

983 **Table 5: HANDEL-ATMS Estimation Performance - SWP and SSR Estimation Module Error Statistics**
984

	POD		FAR	
	SLALOM-CT	HANDEL-ATMS	SLALOM-CT	HANDEL-ATMS
TPW<10 mm T _{2m} <280 K (*)	0.82	0.84	0.19	0.16
TPW<5 mm T _{2m} <250 K	0.64	0.68	0.28	0.23
TPW<3 mm T _{2m} <240 K	0.45	0.54	0.33	0.28

985 Table 6: Comparison between HANDEL-ATMS and SLALOM-CT detection Performances for Different
986 Environmental Conditions (* HANDEL-ATMS working limits).